

1-31-1990

## Formation and characterization of thin superconducting Y-Ba-Cu-O films

Gyusuk Kim  
*New Jersey Institute of Technology*

Follow this and additional works at: <https://digitalcommons.njit.edu/theses>



Part of the [Electrical and Electronics Commons](#)

---

### Recommended Citation

Kim, Gyusuk, "Formation and characterization of thin superconducting Y-Ba-Cu-O films" (1990). *Theses*. 2784.

<https://digitalcommons.njit.edu/theses/2784>

This Thesis is brought to you for free and open access by the Electronic Theses and Dissertations at Digital Commons @ NJIT. It has been accepted for inclusion in Theses by an authorized administrator of Digital Commons @ NJIT. For more information, please contact [digitalcommons@njit.edu](mailto:digitalcommons@njit.edu).

## **Copyright Warning & Restrictions**

The copyright law of the United States (Title 17, United States Code) governs the making of photocopies or other reproductions of copyrighted material.

Under certain conditions specified in the law, libraries and archives are authorized to furnish a photocopy or other reproduction. One of these specified conditions is that the photocopy or reproduction is not to be “used for any purpose other than private study, scholarship, or research.” If a user makes a request for, or later uses, a photocopy or reproduction for purposes in excess of “fair use” that user may be liable for copyright infringement,

This institution reserves the right to refuse to accept a copying order if, in its judgment, fulfillment of the order would involve violation of copyright law.

**Please Note: The author retains the copyright while the New Jersey Institute of Technology reserves the right to distribute this thesis or dissertation**

Printing note: If you do not wish to print this page, then select “Pages from: first page # to: last page #” on the print dialog screen

The Van Houten library has removed some of the personal information and all signatures from the approval page and biographical sketches of theses and dissertations in order to protect the identity of NJIT graduates and faculty.

FORMATION and CHARACTERIZATION  
of THIN SUPERCONDUCTING  
Y-Ba-Cu-O FILMS

by  
1) GYUSUK KIM

Thesis submitted to the faculty of the graduate school of the New  
Jersey Institute of Technology in partial fulfillment of the  
requirements for the degree of

Master of Science in Electrical Engineering

1989<sup>90</sup>

APPROVAL SHEET

Title of Thesis: FORMATION and CHARACTERIZATION  
of THIN SUPERCONDUCTING Y-Ba-Cu-O FILMS

Name and Degree: GYUSUK KIM  
MASTER of SCIENCE in  
ELECTRICAL ENGINEERING  
1989

Thesis and abstract approved: \_\_\_\_\_ 12-22-89  
Dr. KENNETH S. SOHN (Date)  
Professor and Assistant Chairperson of  
Department of Electrical Engineering

Approval of faculty committee: \_\_\_\_\_ 1-10-90  
Dr. ROY H. CORNELLY (Date)  
Professor of Electrical Engineering and  
Director of the Drexler Thin Films  
Research Laboratory

\_\_\_\_\_ 1/11/90  
Dr. MAREK SOSNOWSKI (Date)  
Associate Professor of Electrical  
Engineering

# VITA

Name of candidate: GYUSUK KIM

Permanent address:

Degree and date to be conferred: MSEE, (Dec. 1989) 1990

Date of birth:

Place of birth:

Secondary education: Su Sung High School, Suwon Korea

Collegiate Institutions Attended	Date	Degree
Sung Kyun Kwan University, Korea	1982-1986	BSEE
New Jersey Inst. of Tech., U.S.A.	* 1987-1989	MSEE

Major: Electrical Engineering

Positions held: Research Assistant Sep.88 to Dec.89

New Jersey Inst. of Tech., U.S.A.

## ABSTRACT

Title of thesis: Formation and Characterization of thin superconducting Y-Ba-Cu-O films.

Gyusuk Kim, Master of Science, 1990.

Thesis directed by: Dr. Kenneth S. Sohn

Professor and Assistant Chairperson for

Department of Electrical Engineering.

Thin Y-Ba-Cu-O superconducting films were fabricated reproducibly on MgO (100) substrates by two different processes ; (1) deposition at a low substrate temperature from a single sintered  $\text{YBa}_2\text{Cu}_{3.3}\text{O}_x$  target using RF diode reactive sputtering followed by a post-annealing at around  $830^\circ\text{C}$  ; (2) deposition at the crystallization temperature under oxidizing atmosphere. The superconducting properties of films deposited by process (1) and (2) were studied. The variation of film composition and thickness as a function of distance from the target gas pressure and distance between target and substrate was studied. The Dependence of the film composition and deposition rate on the substrate temperature was studied.

Film crystal structures were characterized by X-ray diffraction using a  $\text{Cu K}\alpha$  source and compositions were determined by Rutherford backscattering spectroscopy ( RBS ). Transition temperature (  $T_c$  ) was determined by four-probe resistance measurement. Parameters for sputter deposition of the highest  $T_c$  Y-Ba-Cu-O films were ; substrate temperature,  $130^\circ\text{C}$ ; sputtering gas mixture, 10 m Torr (10% oxygen 90%

Argon); distance between cathode and anode, 2.5 inch; target power density, 4.87 watts/cm<sup>2</sup>. The deposition rate was in the range of 2.4 - 2.6 nm/min. The post-deposition annealing was carried out under these condition; oxygen pressure > 100 Torr; temperature, 830<sup>o</sup>C for 10 min; warming rate, 2.3<sup>o</sup>C/min; cooling rate, 5<sup>o</sup>C/min. Ba and Cu deficiencies were observed in the films deposited at the crystallization temperature. Post-deposition high temperature treatment results in poor surface morphology, cracking, or undesirable interdiffusion, and limits the choice of substrate material.

It was concluded that the preferred deposition condition for a high quality thin superconducting Y<sup>2</sup>Ba-CU-O films with our RF diode sputtering system is the process (2) using target with Cu and Ba contents increased.



## ACKNOWLEDGEMENTS

I would like to take this opportunity to express my sincere gratitude to Dr. Kenneth S. Sohn for his guidance and cooperation. Without his patience and support, I could have never done this research and thesis.

I would like to express my deep appreciation to Dr. Roy H. Cornely for providing RBS data and technical advice. Film composition analysis in this thesis would have not been possible without his help.

I also acknowledge the financial support provided by the State of New Jersey Commission on Science and Technology and Dr. Walter Kosonocky.

Special thanks are due to the members of the Drexler Microelectronics Laboratory for their cooperation.

# CONTENTS

1. Introduction.	5
2. Technical and scientific background for high $T_c$ superconductor.	
2-1. INTRODUCTION.	7
2-2. BRIEF HISTORY OF SUPERCONDUCTOR.	7
2-3. CRYSTAL STRUCTURES OF Y-Ba-Cu-O SYSTEM AND THEIR SUPERCONDUCTING PROPERTIES.	10
2-3-1. Orthorhombic structure.	10
2-3-2. Tetragonal structure.	14
2-4. THE ROLE OF OXYGEN ON HIGH $T_c$ Y-Ba-Cu OXIDE SUPERCONDUCTOR.	16
3. General techniques for film characterization.	
3-1. FILM THICKNESS AND COMPOSITION MEASUREMENT BY RUTHERFORD BACKSCATTERING (RBS).	
3-1-1. Physical concept of RBS.	19
3-1-2. Experimental instrumentation of RBS.	25

3-2. MEASURING THE STRUCTURE OF FILMS BY X-RAY DIFFRACTION.	
3-2-1. Conceptual theory of X-ray diffraction.	29
3-2-2. Bragg's law.	30
3-2-3. Measurement procedure and determination of lattice type.	31
3-3. ELECTRICAL RESISTANCE MEASUREMENT BY FOUR-PROBE CONTACTS.	34
4. Experimental procedure and sputtering apparatus.	
4-1. INTRODUCTION.	36
4-2. SPUTTERING SYSTEM.	36
4-3. SUBSTRATE PREPARATION.	38
4-4. DEPOSITION PROCESS.	
4-4-1. Deposition process at cooled substrate & following post-annealing process.	39
4-4-2. Deposition process at the crystallization temperature.	41
4-5. HEATER AND SUBSTRATE HOLDER PREPARATION FOR AS-GROWN SUPERCONDUCTING FILM FABRICATION.	42
4-6. FOUR-PROBE CONTACT PREPARATION.	43

## 5. Experimental results and discussion.

5-1. INTRODUCTION.	44
5-2. SUBSTRATE TEMPERATURE EFFECT.	44
5-2-1. Effect of substrate temperature on the film composition and deposition rate.	45
5-2-2. Effect of substrate temperature on the temperature dependence of electrical resistance.	49
5-3. EFFECT OF RADIAL POSITION AND RESPUTTERING ON THE FILM COMPOSITION AND THICKNESS.	51
5-4. EFFECT OF GAS PRESSURE ON THE FILM COMPOSITION AND THICKNESS.	57
5-5. EFFECT OF TARGET DISTANCE ON THE FILM COMPOSITION AND THICKNESS.	59
5-6. ANNEALING EFFECT ON THE TEMPERATURE DEPENDENCE OF ELECTRICAL RESISTANCE.	63

## 6. Conclusions and suggestions for future work.

6-1. CONCLUSIONS.	65
6-2. SUGGESTIONS FOR FUTURE WORK.	66
REFERENCE	68

APPENDIX	A	70
APPENDIX	B	75
APPENDIX	C	79
APPENDIX	D	86
APPENDIX	D	93
APPENDIX	F	97

# 1. INTRODUCTION

The research reported in this thesis was part of the 1988 Innovation Partnership Program of NJIT on "High  $T_c$  Superconductors". All the experiments were carried out under the supervision of Dr. K. S. Sohn, Dr. R. Cornely and Dr. L. Suchow at Drexler Microelectronics, Superconductivity Research laboratories, Electrical Engineering and Chemistry Department; NJIT, funded by an innovation partnership grant given by the New Jersey commission on Science and Technology.

The primary goals of this research were to develop a technology for reproducible fabrication of thin superconducting films and characterize the films.

The brief history of superconductor, crystal structures of Y-Ba-Cu-O system and superconducting properties are in Chapter 2. The quality of the films determined by structure and composition of the films.

In Chapter 3, general techniques for characterizing the films are discussed.

Chapter 4 details the experimental procedure and techniques for preparation of the sputtered films. The description of the sputtering apparatus is also discussed in this chapter.

Experimental data and results obtained are presented in Chapter 5. A comprehensive discussion on the results is also presented in this chapter.

Finally, concluding remarks and suggestions for future work are presented in Chapter 6.

## 2. TECHNICAL & SCIENTIFIC BACKGROUND FOR HIGH $T_c$ SUPERCONDUCTOR

### 2-1 INTRODUCTION

This chapter presents crystal structures of Y-Ba-Cu-O system, tetragonal and orthorhombic and describes the role of oxygen on high  $T_c$  Y-Ba-Cu-O superconductor. The purpose of this overview is to describe the criteria for high  $T_c$  Y-Ba-Cu-O superconductor.

### 2-2. BRIEF HISTORY OF SUPERCONDUCTOR

Since the discovery of superconductivity by Kammerlingh Onnes in 1911 in Hg at 4.2 K, one of the primary objectives of superconductivity research has been to raise the transition temperature  $T_c$ . By almost any criterion, progress was slow. The discovery of  $T_c$  above 10 K in NbC and NbC was one breakthrough, The discovery of the A15 compounds, with  $T_c$  finally breaking through the 20-K barrier in the late 1960s and early 1970s, represented the culmination of two decades of intense search for higher transition temperatures. This research involved extensive investigations of materials properties and gave rise to "Matthias's Rules" (Hulm and Blaugher, 1972) for promoting higher values of  $T_c$ :

- (1) Cubic transition metals are best.
- (2) Niobium is the best transition metal.
- (3) Certain values of electron/atom ( $e/a$ ) ratio are special.



(4) High  $T_c$ 's lie in the regime of lattice instabilities.

Certain aspects of these rules have been understood on a basic level; for example, in the cubic transition metals, the transition-metal carbonitrides, and the A 15 compounds, this special  $e/a$  ratios (roughly 4.7 and 6.5) correspond to regions of high density of states  $N(E_F)$  at the fermi level  $E_F$ . Niobium not only tends to lead to  $e/a$  ratios near 4.7, but also lies near the center of the transition-metal series where the electron-phonon interaction is strongest. These trends have been reviewed by Klein and Pickett (1983). In addition, it became clear that both high- $T_c$  and lattice instabilities arise from strong electron-phonon interactions so they tend to occur together. However, there is no definite causal relationship between lattice instability and high  $T_c$ . Contrary to early speculations, the best estimates now seem to indicate that low phonon frequencies contribute little to high values of  $T_c$ .

The breakthrough in higher  $T_c$ 's resulted from Bednorz and Muller's discovery (1986) in the copper oxide system. they were convinced that it was necessary to move beyond the standard high- $T_c$  classes to obtain a real breakthrough. They chose to work on transition metal oxides, both because they were different and because they often displayed polaronic effects typical of extremely strong electron-phonon interactions. In 1986 they found evidence of a superconducting transition occurring near 30 K in the La-Ba-Cu-O

system, a result that was rapidly confirmed and refined by a number of laboratories in the U.S., Japan, and Europe. It was established that  $T_c$  in the range 20-40 K occurs for  $\text{La}_{2-x}\text{M}_x\text{CuO}_{4-y}$ , with  $\text{M} = \text{Ba}, \text{Sr}, \text{Ca}$ , and that application of pressure leads to a large pressure coefficient of  $T_c$  and drives  $T_c$  above 50 K in the  $\text{M} = \text{Sr}$  system.

The replacement of La by Y in LBCO produced in early 1987 a 90-K superconductor, later identified as  $\text{YBa}_2\text{Cu}_3\text{O}_{7-y}$ . Like the initial system, this material was prepared by ceramic processing techniques. High-temperature annealing in an oxygen-containing atmosphere was necessary to produce the oxygen content and the crystalline phase necessary to give high  $T_c$ . Although other growth techniques have now been found that result in the high- $T_c$  phase, it was clear from preparations considerations that the new copper oxides were completely different from the previous high-temperature superconductors.

Although there were numerous reports of resistive and magnetic anomalies at much higher temperatures, the next breakthrough came in early 1988 with the discovery by Maeda et al. (1988) and Chu et al. (1988) of  $\text{Bi}_2\text{Sr}_2\text{CaCu}_2\text{O}_{8-x}$ .

This Bi-based compound not only showed the onset of superconducting around 110 K, but also contained no rare-earth element. It was also distinguished by its highly micaceous nature, indicating more pronounced layering than its predecessors. This breakthrough was followed rapidly by the discovery by Sheng et al. (1988) of onsets at 115 K in the Tl-Sr-Ca-Cu-O system was soon

improved to above 120K by several groups. The superconducting phase was identified as  $Ti_2Ba_2CaCu_2O_{8-y}$ . The crystal structures of these systems were identified and found to share certain features in common with the La-M-Cu-O and Y-Ba-Cu-O materials, particularly the existence of square Cu-O layers separated by more-or-less ionic regions.

### 2-3. CRYSTAL STRUCTURES OF Y-Ba-Cu-O SYSTEM AND THEIR SUPERCONDUCTING PROPERTIES.

Great efforts have been made to understand the physics of the high  $T_c$  oxide superconductor, Ba-Y-Cu-O.<sup>(1,2)</sup> However, the superconducting properties ( such as  $T_c$ , resistive transition curve and its magnetic field dependence, and critical current ) and resistivity in the normal state are known to differ from sample to sample. In principle, these seemingly complicated behavior can be attributed to the different types of crystal structure involved, i.e. tetragonal and orthorhombic. Although the difference in the structure is minor indeed, it is true that their electronic properties are quite different.

#### 2-3-1. Orthorhombic structure

Following the discovery by Wu et al. (1987) of  $T_c$  above 90 K in the YBCO system, a large number of papers reported on the crystal structure of this class of materials. The high-temperature superconducting phase of  $YBa_2Cu_3O_7$  forms in an orthorhombic Pmmm

structure with a single formula unit per primitive cell. The structure is about as simple as conceivable for a quaternary compound with ratios 1:2:3:7. It can be viewed as a defect perovskite lattice  $(Y-Ba)_3Cu_3O_{9-x}$  based on three Cu-centered perovskite cubes with both O vacancy ordering and Y-Ba ordering along the axis. Of the two O vacancies ( $X = 2$ ), one occurs in every third Cu-O plane, along the a axis, at the site  $(1/2,0,0)$ , resulting in the orthorhombic (rather than tetragonal) symmetry. The Y and two Ba ions are ordered along the c axis, and the other O vacancy occurs in the Y plane. The structure is illustrated in Fig.1. The space group is Pmmm (No. 47 in the International Tables).

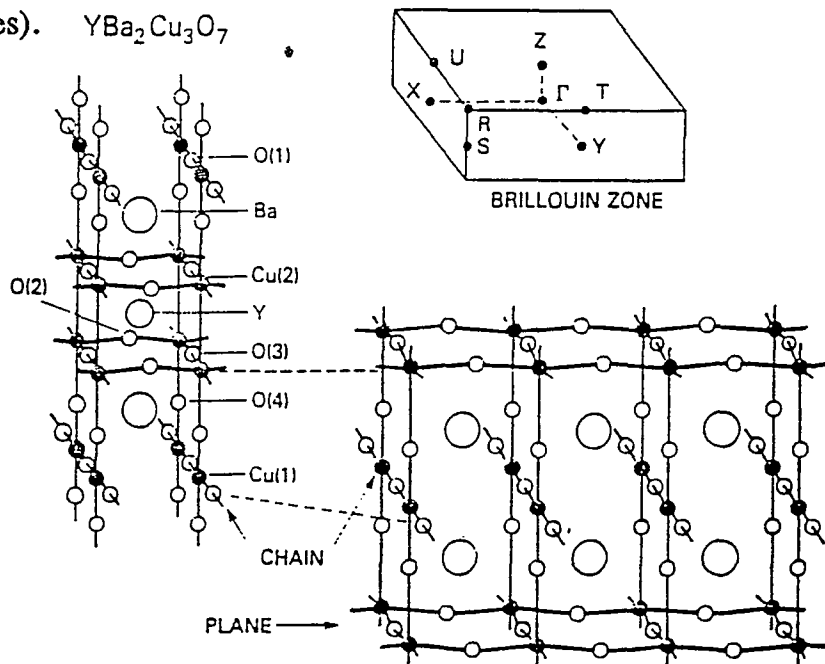


Figure 1. Crystal structure of  $YBa_2Cu_3O_7$ , illustrating the CuO chains and the  $CuO_2$  planes. Also shown is the corresponding simple orthorhombic Brillouin zone, with symmetry points marked.<sup>(3)</sup>

The resulting structure is usually described in terms of Cu-O planes or layers and Cu-O chains. The chains consist of Cu1 and O1 atoms along the b axis, at (0,0,0) and (0,1/2,0), respectively, (using common but by no means universal notation for the site). These chains are more properly regarded as ribbons, however, since the O4 atom lies above and below the Cu1 atom at the (0,0, $z_{O4}$ ) position, and the Cu1-O4 separation is the smallest Cu-O distance in the structure. Thus the Cu1 atom is fourfold coordinated with O ions, and each O1 ion is shared by two Cu1 atoms.

The layers consists of Cu2 sites at (0,0, $z_{Cu2}$ ) neighbored by O2 and O3 sites at (1/2,0, $z_{O2}$ ) and (0,1/2, $x_{O3}$ ). The heights are, in units of c, given by  $z_{Cu2} = 0.3574$ ,  $z_{O2} = 0.3767$ , and  $z_{O3} = 0.3804$ , according to Jorgensen, Beno, et al. (1987), who also report  $z_{O4} = 0.1542$ ,  $a = 3.8591$  A,  $b = 3.9195$  A,  $c = 11.8431$  A. The Cu-O layers are therefore somewhat dimpled, with two oxygen O2 and O3 being nearly coplanar, but with the Cu2 site lying out of this plane by  $0.022c = 0.25$  A. The Cu2 displacement out of the O2-O3 plane is toward the O4 site; however, the Cu2-O4 distance is still large (2.38 A) compared to the Cu1-O4 distance of 1.78 A.

With Cu1 chosen at the origin, as was done here, the Y site is at (1/2,1/2,1/2) and the Ba site is at (1/2,1/2, $z_{Ba}$ ), with  $z_{Ba} = 0.1895$ . Thus the Ba and O4 sites form a warped rocksaltlike layer between the layers and the chains. Oxygen atoms are entirely missing from the Y layers, which separate the Cu-O layers in the unit cell. For later

reference we list the site symmetries: Cu1, O1, and Y: mmm; Cu2, O2, O3, O4, and Ba: mm.

Fig 2 shows the electrical resistance of YBCO film as a function of temperature. The sample shows a metallic character with a sharp transition at 45 K. This indicates a homogeneous superconducting phase.

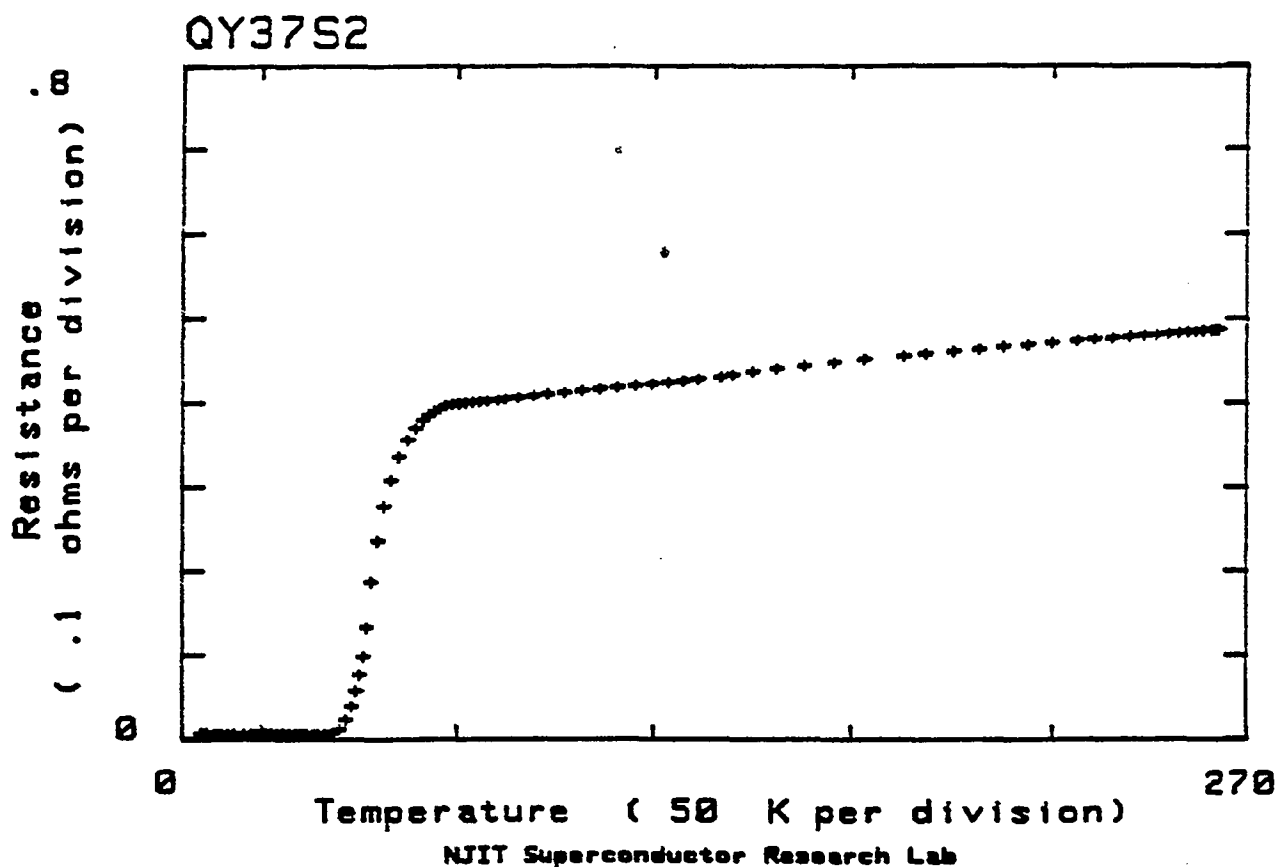


Figure 2. Electrical resistance of a homogeneous superconducting phase of YBCO as a function of temperature.

### 2-3-2. Tetragonal structure

For lower oxygen concentrations, which can be obtained by appropriate heat treatment, the structure assumes tetragonal symmetry. Moreover, at elevated temperature the material with high oxygen concentrations assumes the same tetragonal symmetry. The ideal symmetry of these phases can be described in terms of the composition  $\text{YBa}_2\text{Cu}_3\text{O}_6$ , whose structure differs from the orthorhombic Pmmm structure described above by the removal of the O ion from the chain O1 site. With the O1 site empty, it becomes equivalent to the O5 orthorhombic site, which corresponds in  $\text{YBa}_2\text{Cu}_3\text{O}_7$  to the vacancy at  $(1/2,0,0)$ . The resulting structure is pictured in Fig.3.

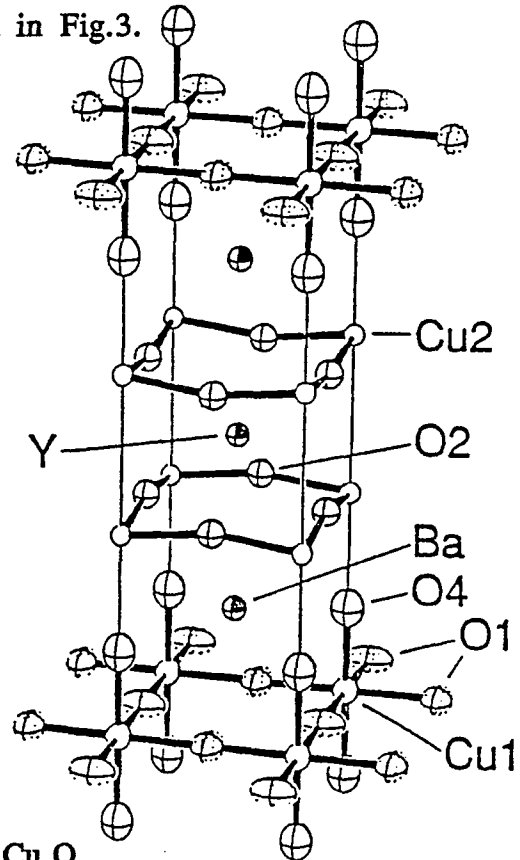


Figure 3. Tetragonal structure of  $\text{YBa}_2\text{Cu}_3\text{O}_6$ .

The high-oxygen-concentration material assumes the same symmetry at high temperature as the result of an order-disorder transformation, in which the ions on the O1 sites randomly occupy both the O1 and O5 sites, resulting in average tetragonal symmetry.

The resulting space group is P4/mmm (No.123 in the International Tables), with  $a = 3.863 \text{ \AA}$ ,  $c = 11.830 \text{ \AA}$  reported by Swansea and Stein Fink (1987) for material near the stoichiometric composition (i.e., O6). These authors also report  $z_{\text{Ba}} = 0.1934$ ,  $z_{\text{Cu2}} = 0.3604$ ,  $z_{\text{O4}} = 0.1533$ , and  $z_{\text{O2}} = 0.3793$  (O2 and O3 become equivalent). Thus the internal structural parameters appear to change very little as a result of the loss of the O1 ion. The site symmetries are Cu1, Cu2, and Y: 4/mmm; O1: mmm; O2: mm; O4 and Ba: 4mm.

Several studies have been made of the effect of intermediate oxygen concentrations between  $n = 6$  and  $n = 7$  upon the crystal structure. The structure changes from orthorhombic to tetragonal in the range  $n = 6.35-6.65$ , depending on the preparation of the material. If samples are cooled slowly, the oxygen vacancies strongly tend to order, while rapid cooling inhibits the ordering. If the vacancies order, the orthorhombic symmetry can be retained to lower vacancy concentration than if the vacancies are disordered.

Fig.4 shows the electrical resistance as a function of temperature. The sample exhibits the semiconductor-like character and shows the very high resistance at low temperature.



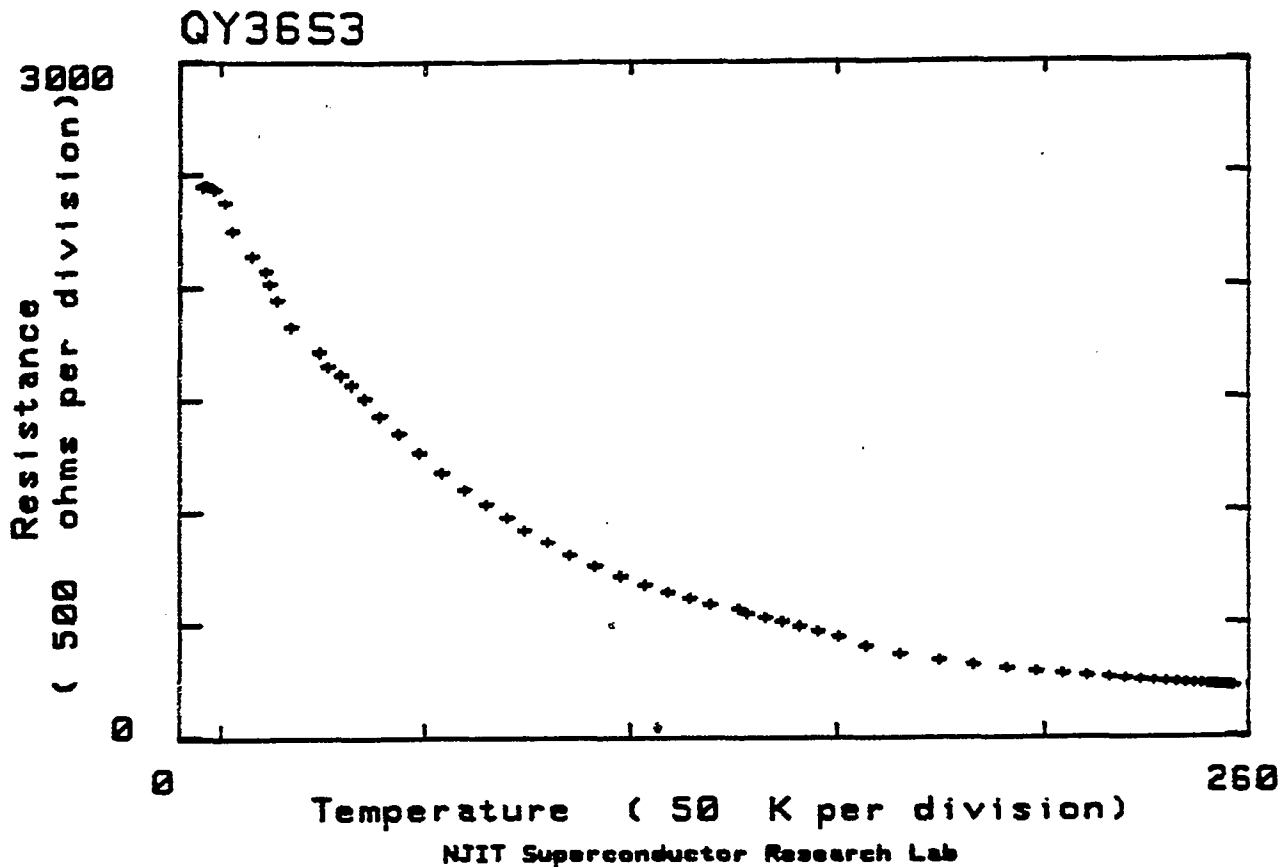


Figure 4. Electrical resistance of a tetragonal phase of YBCO as a function of temperature.

#### 2-4. THE ROLE OF OXYGEN ON HIGH $T_c$ SUPERCONDUCTOR

The relation between the oxygen deficiency  $x$  and the two polymorphs of  $Y_{1.2}Ba_{1.8}Cu_3O_{6.7-x}$ , i.e., orthorhombic and tetragonal phases, have been studied<sup>4</sup> by the gravimetric method combined with the X-ray diffraction analysis. The oxygen deficiency  $x$  was varied by

annealing the samples in an argon or oxygen atmosphere at an appropriate temperature, followed by rapid quenching to room temperature. It is shown that the tetragonal phase is characterized by a large oxygen deficiency,  $x = 0.6-0.7$ .<sup>6</sup> Recently extensive efforts have been done on the identification of superconducting phase in Y-Ba-Cu oxide. Through these efforts it becomes clear that the orthorhombic phase with composition  $YBa_2Cu_3O_{6.7}$  is responsible for the superconductivity. However, a tetragonal phase is often found depending on the method of heat treatment; this phase is most pronounced in a specimen quenched from high temperatures. From these facts it is deduced that the tetragonal phase is stable at higher temperatures and the oxygen content of this phase should be smaller than the superconducting orthorhombic phase. When annealed at temperatures between  $920^\circ\text{C}$  and  $1000^\circ\text{C}$  the crystal structures of these films are orthorhombic, while when annealed at  $1010^\circ\text{C}$  the structures are tetragonal. Superconductivity can be observed for the orthorhombic films. Their critical temperature of superconducting transition becomes higher as the a-axis becomes shorter, and is independent of the b-axis value.<sup>5</sup>

A study of precise oxygen concentration dependence of the superconducting volume fraction in  $YBa_2Cu_3O_x$  ( $6.22 \leq X \leq 6.96$ ) revealed the phase diagram of this superconducting system. Three characteristic phases are found based on the oxygen concentration: (1) a nonsuperconducting tetragonal phase for  $6.2 < X < 6.4$ , (2) a

low- $T_c$  (55-70 K) orthorhombic phase for  $6.4 \leq X < 6.8$  and (3) a high  $T_c$  (90 K) orthorhombic phase for  $6.8 \leq X < 7.0$ . Evidence for a distinct critical concentration at  $X = 6.7-6.8$ , necessary to sustain the bulk high- $T_c$  ( 90 K ) superconductivity has been presented.<sup>6</sup>

### 3. GENERAL TECHNIQUES FOR FILM CHARACTERIZATION

#### 3-1. Film thickness and composition measurement by Rutherford backscattering (RBS).

##### 3-1-1. PHYSICAL CONCEPTS OF RBS

Rutherford back-scattering is a widely used surface analysis technique in many branches of materials science.<sup>7,8</sup> A beam of energetic ions is directed at the solid under investigation. The ions collide elastically with lattice atoms within the sample and are scattered back into a suitable detector which counts the number of scattered particles and measures their energy. The information contained in the scattered particles spectra can be interpreted to give, data on the composition of the sample, the distribution of elements within the sample and the sample thickness.

Rutherford back-scattering has long been used for surface analysis by nuclear physicists, since it provides a quick and simple method of examining target purity and thickness in nuclear physics experiments. In the last 20 years, however, the growing need for surface analysis in many areas of materials science has prompted rapid expansion in the development and use of RBS. Many accelerators in the 1-3 MeV energy regime, that were previously used for nuclear physics, experiments are now used for solid state analysis by RBS. The

electronic industries have provided the largest driving force for the development of RBS techniques, with their requirements for detailed information on shallow doped layers in semiconductors and on metal-semiconductor contacts. The RBS technique is now extensively employed in a number of fields ( see, for example, J.R. Bird & G.J.Clark, 1981 ).

A schematic RBS spectrum is given in Fig.5. The analyzing beam of energy,  $E_0$ , strikes a sample containing two elements of masses, A, and, B. Particles back-scattered from target atoms at the surface have an energy, after collision of either  $E_A$  or  $E_B$  depending on the type of target atom from which they scatter. The energy after collision is related to the energy  $E_0$  collision by a constant  $K$  which depends on the mass of the struck atom. Thus  $E_A = K_A E_0$  and  $E_B = K_B E_0$ . The constants  $K_A$  and  $K_B$  can be calculated for a given projectile/target combination and for a given scattering geometry. Consequently the signals appearing on the energy scale of Fig.5 at positions  $E_A$  and  $E_B$  can be identified as coming from masses A and B, respectively, and the energy scale is thus converted into a mass scale.

Only a small fraction of the beam will be scattered by surface atoms. Further scattering occurs from atoms located at successively deeper layers below the surface. In each case the collision can be treated as a binary collision and the energy immediately after such a collision is related to the energy immediately before the collision via the kinematic constant,  $K$ . In moving through a sample to reach the

depth at which it elastically scatters, an ion loses energy inelastically. Passing back through the sample the ion continues to lose energy inelastically. The rate of inelastic energy loss is known for many ion-target combinations. As shown in Fig.5, scattering from A atoms which are below the surface will give signals at energies less than  $K_A E_0$ . The energy scale of Fig.5 can therefore also be converted to a depth scale. A single RBS spectrum consequently provides both mass identification and the depth distribution of these masses.

The number or yield of scattered particles depends principally on the Rutherford collision cross-section. The ion experiences simple Coulomb repulsion which is accurately and quantitatively described by the Rutherford cross-section. The yield of scattered particles in the RBS spectrum of Fig.5 can thus be converted to give quantitative data on target composition.

By combining RBS analysis with channelling, further information on the state of surfaces and surface layers becomes possible. A projectile can be directed to enter a crystal lattice in a low index direction. Many of the ions entering in such a direction pass down the open channels of the crystal and do not come sufficiently close to lattice atoms to elastically collide and be back-scattered. The RBS yield for single crystals therefore depend on the angle between the analyzing beam and the lattice of the sample.

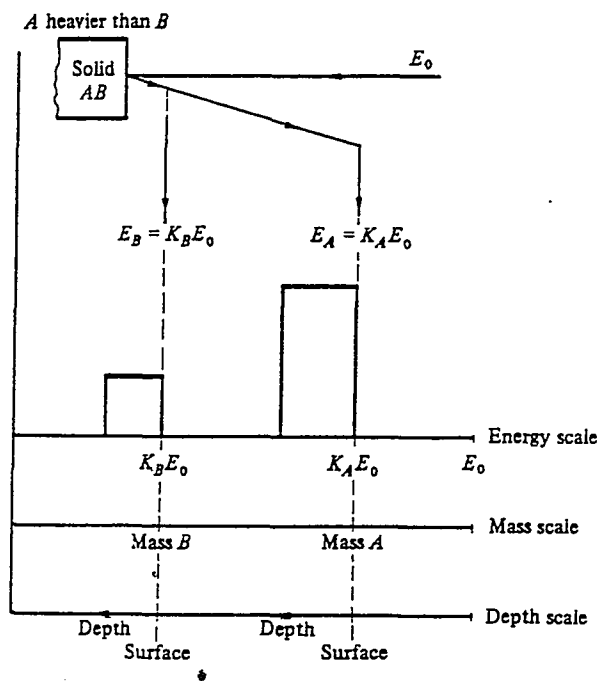


Figure 5. Rutherford backscattering from a solid composed elements of mass A and B

The combination of RBS and channelling can provide data on the degree of disorder within a single crystal and the lattice position of impurities within the lattice. In addition, in experiments conducted under UHV conditions, measurements can be made of the relaxation in position of crystal surface atoms and the reconstruction that can occur on certain crystal faces.

---

## RUTHERFORD BACKSCATTERING

### \* Advantages

Ability to detect hydrogen using recoil analysis.

Concentration-depth profiles without the need to strip the sample.

Absolute quantification to better than 5%. Increased accuracy with calibration standards.

High reproducibility of results.

Virtually non-destructive (except for polymers and biological materials).

Associated technique of ion channelling provides useful structural information on single crystals.

### \* Disadvantages

Essentially a broad area technique with only limited capability for small area analysis.

Comparatively poor surface sensitivity ( 50 Å at best, but typically 200 Å ).

Elemental analysis only ( no chemical bonding information ).

Wide range of sensitivities ( overcome to some extent by using associated techniques such as nuclear reaction analysis ).

Comparatively high capital investment and limited commercial availability.

---

The interaction between the projectile and target atom can be



described as an elastic collision between two isolated particles. The energy of the projectile after the collision can be related to its energy before the collision by means of a kinematic factor  $K$ . The likelihood that scattering will occur, i.e. the probability of scattering, depends on the scattering cross-section. As the projectile passes through the scattering medium it suffers an average energy loss  $dE/d$  and this leads to the concept of the stopping cross-section. Finally, since there are statistical fluctuations in the energy loss of a projectile as it penetrates a solid, particles entering a solid with a given energy will not have identical energies after travelling the same distance. This phenomenon is called energy straggling.

The above four basic physical concepts form the basis of RBS. The kinematic factor  $K$  leads to the ability for mass analysis. The scattering cross-section provides RBS with a quantitative capability. The stopping cross-section results in the capability for depth analysis and energy straggling sets limits on mass and depth resolution.

### 3-1-2. EXPERIMENTAL INSTRUMENTATION OF RBS

A schematic of the equipment used in RBS is shown in Fig.6. A high-energy beam, typically 2MeV  ${}^4\text{He}^+$ , is extracted from a suitable accelerator and passed through a magnetic analyzer. The beam is then collimated and directed onto the target. Ions which are back-scattered

into a particular solid angle are detected by a solid state detector. The number and the energy of the particles striking the detector is stored electronically.

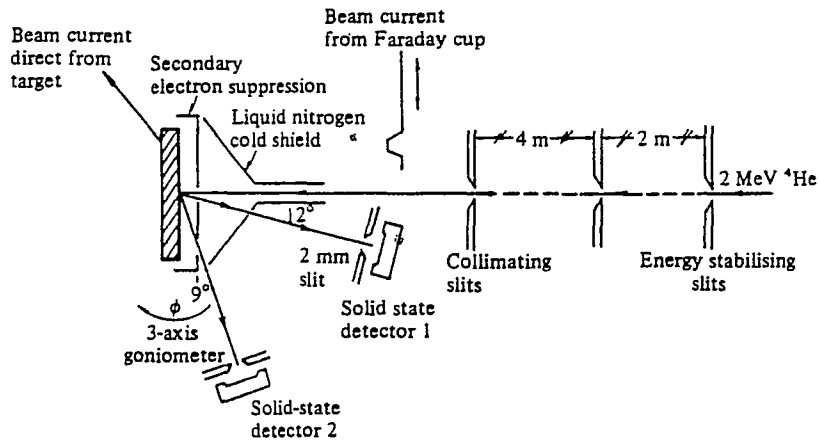


Figure 6. Experimental arrangement for RBS.

The commonest form of accelerator used for RBS is based on the electrostatic Van de Graaff generator. The high voltage ( typically several MeV ) at the accelerator terminal is produced by means of a rapidly moving insulating belt that conveys charge between ground

potential and the terminal. Ions are extracted from an RF ion source and accelerated down an acceleration column that is maintained at  $10^{-6}$  torr. The column and the high voltage terminal are surrounded by a tank which is pressurized to provide high-voltage insulation. The discharge current between a series of sharp points (corona points) and the high-voltage terminal is monitored and used as a controllable load to stabilize the terminal voltage.

RBS requires a highly energy-stabilized ( $\pm 2$  KeV) ion beam. Fluctuations in the terminal voltage can be corrected by feedback systems. A common method is to sample the beam, after magnetic analysis, using high and low-energy slits. A change in the terminal voltage causes the beam to shift its spatial position on leaving the magnet with a corresponding increase in the current to one of the two slits. The slit signals are used to control the terminal voltage via the corona discharge current. The energy of the accelerator can be calibrated using nuclear resonance reactions. Reactions such as  $^{27}\text{Al}(p,\gamma)^{28}\text{Si}$  occur at precisely known beam energies and provide absolute energy calibration.

The  $^4\text{He}^+$  ion beam from an ion source is often accompanied by  $^{16}\text{O}^+$  ions. If these latter ions lose a another electron after acceleration down the column, but before magnetic analysis, they will not be separated from the  $^4\text{He}^+$  beam. This contamination interferes with RBS analysis by giving spurious signals at the lower energies in spectra and by causing radiation damage in single crystals in channelling

experiments. The ion current that strikes the target is measured and integrated. For accurate measurements care must be taken to suppress secondary electrons at slits and at the target. (Alternatively, the current can be measured using a Faraday cup.) In many RBS measurements, relative rather than absolute measurement of ion fluence is sufficient.

The scattered beam is energy analyzed and counted. The highest energy resolution is provided by magnetic analysis but data accumulation is slow since only a single energy is measured for a specific magnetic field strength. Solid state detectors are more commonly used since they detect particles of all energies simultaneously. In a typical experimental arrangement a silicon surface barrier detector (area  $25\text{mm}^2$ ) is placed at a scattering angle of  $170^\circ$  and a distance 15 cm from the target. The angular spread of the beam at the detector can be reduced by placing slits in front of the detector.

The initial stage of signal amplification is a charge-sensitive preamplifier which provides a minimum of pulse shaping but preserves a maximum signal-to-noise ratio. The subsequent main amplifier creates a suitable pulse shape to optimize resolution and counting-rate. The shaping produces individual pulses whose amplitudes are proportional to energy. The shaping helps to eliminate pulse-pile up which occurs if the spacing between pulses is small such that they overlap and cause erroneous amplitude measurements. Data acquisition, storage and

display is usually provided by a multichannel analyzer (MCA) which is essentially a dedicated microcomputer. The commonest mode of operation of the MCA is pulse-height-analysis (PHA). The desired RBS spectrum is accumulated by measuring the amplitude of each signal (caused by a scattered particle striking the detector) and storing it at an appropriate channel-address (or channel number) that is proportional to the pulse height. RBA spectra commonly require 512 channels and so a memory of 4096 channels permits storage of eight spectra at one time. An alternative mode of operation for the MCA is the multi-channel-scaling mode (MCS). An individual channel counts all the incoming data for a predetermined time interval. During subsequent intervals counting is transferred to the next channel. This mode of operation is useful in channelling experiments in which the RBS yield is measured repeatedly at various angles of the analyzing beam relative to a crystal channelling direction.

The pressure in the target chamber is typically  $10^{-6}$  torr although surface studies combined with channelling require UHV conditions, i.e.  $< 10^{-9}$  torr. It is possible to produce a UHV environment by placing a cryo-shield around the target which is otherwise in a low ( $10^{-6}$  torr) vacuum system. Low pressures help to reduce contamination on the target surface from hydrocarbons which are dissociated by the  $^4\text{He}$  beam to form an adherent carbon layer.

For standard RBS measurements simple target holders which contain a number of samples that can be rotated into the analyzing beam are

sufficient. Channelling experiments require crystals to be oriented with respect to the beam and this involves use of a goniometer. A three-axis goniometer, providing tilt in two planes combined with 360° rotational movement, is commonly used. Stepping motors drive each of the three-axes in small, 0.01°, angular steps. In channelling experiments the RBS yield is monitored as a function of sample orientation relative to the beam. Repeated measurements at different angles are used to orient the crystal to a position such that the beam is directed in a low index crystallographic direction. All the RBS experiments were done by Dr. Cornely at Bell Core, Red bank.

## 3-2. Measuring the structure of films by x-ray diffraction.

### 3-2-1. THEORY OF X-RAY DIFFRACTION.

One method used to reveal the crystal structure of materials is the X-ray diffraction method.<sup>9,10</sup> This is a highly accurate method of structural investigation and it offers many benefits over other methods, it requires very small amounts of sample, it requires little time to perform the measurement, and it is a nondestructive method. A sample is placed in an intense X-ray beam. The detector is then rotated through various angles while the beam reflected by it is being measured in a fixed detector with a wide slit. The resulting graph of intensity versus the angle, which is recorded on a chart operated by the detector.

### 3-2-2. BRAGG'S LAW

By general laws of physics the angle of incident equals the angle of diffraction. The Bragg angle  $\theta$  is defined as the angle which the incident beam or the diffracted beam makes with the  $hkl$  plane of the crystal which satisfies Bragg's law:

$$\lambda = 2d_{hkl}\sin\theta$$

where

$\lambda$  = Wavelength of the diffracted radiation,

$\theta$  = The Bragg angle, and

$d$  = Distance between the two parallel planes with

\* Miller indices  $h,k,l$  \*

#### \* MILLER INDICES

[ The plane with Miller indices  $h$ ,  $k$ , and  $l$  makes intercepts  $a/h$ ,  $b/k$ , and  $c/l$  with the unit cell axes  $a$ ,  $b$ , and  $c$ .

The "law of rational indices" states that the indices of the faces of a crystal are usually quite small integers, seldom greater than three. The importance of the Bragg equation is that it identifies the integers  $h$ ,  $k$ ,  $l$  that specify the "order" of diffraction in the Laue equations with the Miller indices of the lattice planes causing the "reflection". ]

Since the wavelength of the radiation is known, the crystal dimensions and geometry can be determined from knowing diffraction patterns at several diffraction angles. The arrangements of atoms within the unit cell can only be determined from the intensity measurements of the radiation in each diffraction spot. This is then compared with the theoretically predicted density for several possible arrangements in the unit cell. The geometry of the lattice determines the geometry of the diffraction pattern and distribution of atoms in a lattice determines the intensities of various diffraction spots.

### 3-2-3. MEASUREMENT PROCEDURE AND DETERMINATION OF LATTICE TYPE.

To get a clearer understanding of the resultant intensities that occur at different Bragg angles, the following theory is discussed. Consider a beam of perfectly parallel monochromatic x-rays of wavelength  $\lambda$  incident on a crystal at an angle  $\theta$ , called the Bragg angle, where  $\theta$  is measured between the incident beam and the  $hkl$  crystal planes under consideration.

The basic procedure for finding the interplanar spacing of a crystal is as follows:

- 1) Find angle  $2\theta$  where the intensity peak is observed.
- 2) Find the line corresponding to this angle  $2\theta$  from the tables.

If this review is not available simply use the Bragg equation:



$$d = \frac{\lambda}{2\sin\theta} \quad (\text{eq.1})$$

Where in our case  $\lambda = 1.5405$  Angstroms and  $\theta$  is determined from the location of the intensity peak.

When the interplanar spacing is found from the measurements, it must then be compared to the theoretical value for accuracy and precision considerations. The intensity peak amplitude and its area determine the structure and orientation of the samples.

\* EXAMPLE \*

Let us think about two types of silicon with different orientations. One has orientation of  $\langle 111 \rangle$  the other one has  $\langle 400 \rangle$ . The silicon samples with orientation  $\langle 111 \rangle$  shows a major intensity peak at 28.4 degrees and a minor peak at 25.6 degrees. The lower peak is caused by the Copper  $K\beta$  radiation. For the Bragg angle of 28.4 the interplanar spacing is calculated from equation to be:

$$d = \frac{\lambda}{2\sin\theta} = \frac{1.5405}{2\sin(28.4/2)} = 3.1399 \text{ \AA}$$

The  $K\beta$  radiation can also be used to derive this information with the change of its wavelength into the above equation. Now we can use ( eq.2 ) to get the quadratic sum of the Miller indices which helps to find the orientation of

this sample.

$$d = \frac{a}{\sqrt{h^2+k^2+l^2}} \quad (\text{eq.2})$$

$a$  = Lattice constant ( for Si  $a$  = 5.4309 A )

$$h^2+k^2+l^2 = \left(\frac{a}{d}\right)^2 = \left(\frac{5.4309}{3.1399}\right)^2 = 2.9927$$

The closest whole number to this value is 3 which yields.

$$h = 1$$

$$k = 1$$

$$l = 1$$

Therefore the sample must have an orientation of  $\langle 111 \rangle$ .

For the second type of Silicon the intensity peaks occurred at 61.8 degrees and 69.3 degrees with the latter as the dominant ray which is the Cu  $K\alpha$  radiation. Using equation ( eq.1 ) yields:

$$d = 1.3564 \text{ A}$$

This interplanar spacing is different from the previous sample's spacing because of the orientation difference. From ( eq.2 ) the quadratic sum of the Miller indices is found to be:

$$h^2 + k^2 + l^2 = 16.0313$$

Taking the closest whole number for the Miller indices under diamond cubic structures having values of 16, following results are obtained:

$$h = 4$$

$$k = 0$$

$$l = 0$$

So the Silicon sample must have a  $\langle 400 \rangle$  orientation which is the same as having an orientation of  $\langle 100 \rangle$ .

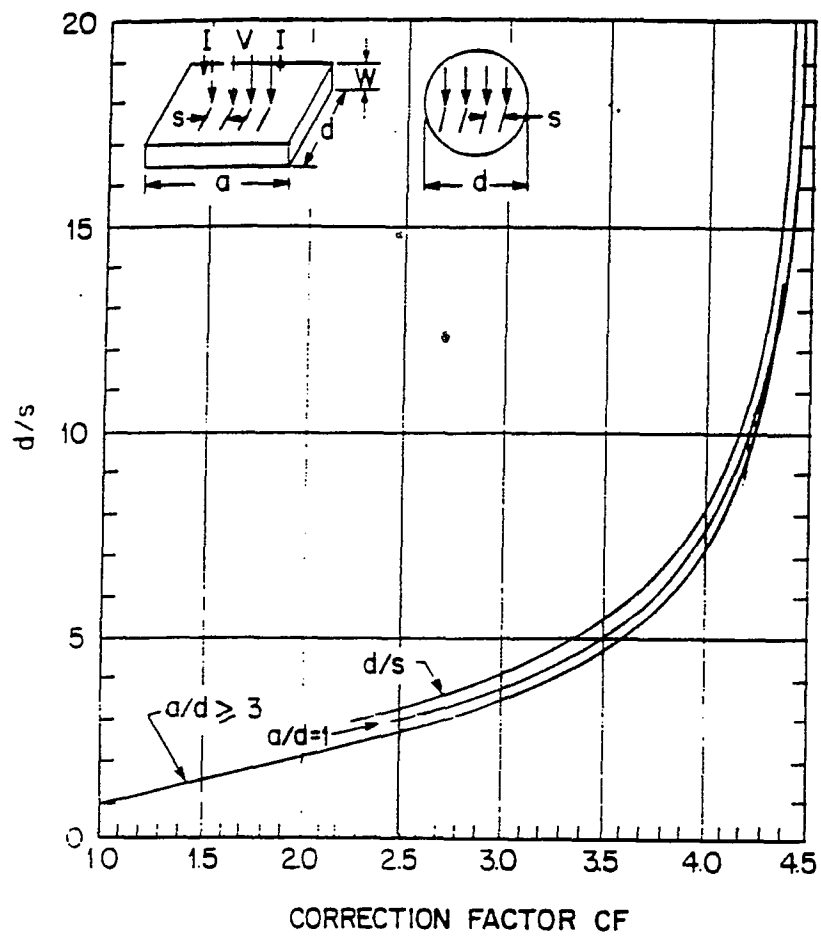
### 3-3. Electrical resistance measurement by four-probe contacts,<sup>(11)</sup>

The most common method for measuring resistivity is the four-point probe method shown in the insert of Fig.7. The probes are equally spaced. A small current from a constant-current source is passed through the outer two probes and the voltage is measured between the inner two probes. For a thin film sample with thickness  $W$  much smaller than either  $a$  or  $d$ , the resistivity is given by

$$\rho = \frac{V}{I} \times W \times CF \quad \Omega\text{-cm}$$

where  $CF$  is the correction factor shown in Fig.7. At the limit when  $d \gg s$ , where  $s$  is the probe spacing, the correction factor becomes  $\pi/\ln 2 = 4.54$ .

Figure 7. Correction factor for the measurement of resistivity using a four-point probe.



## 4. EXPERIMENTAL PROCEDURE AND SPUTTERING APPARATUS

### 4-1. Introduction

The sputtering apparatus is described and the experimental procedure is explained in this chapter. Two different processes are presented: (1) deposition at a low substrate temperature followed by a post-annealing at around 830°C; (2) deposition at the crystallizing temperature.

### 4-2. Sputtering system

A modified version of MRC 8800 sputtering system was used for the deposition of Y-Ba-Cu-O thin films. The method of sputtering involved Radio Frequency (RF) sputtering in a diode configuration. A schematic representation of the sputtering system is shown in Fig.8. The RF generator, which operates at 13.56 MHz, supplies voltage to an  $\text{YBa}_2\text{Cu}_{3.3}\text{O}_x$  target, 2.25 inch in diameter and 0.25 inch thickness. The rotating target head can accommodate four targets fitted with ground shields. The substrates are laid on a 0.25 inch thick platen in the intervac chamber and then, are transported into the main chamber without breaking vacuum in main chamber. The distance between anode and cathode can be varied from 1.8 inch to maximum 3.6 inch. The main vacuum chamber is made of stainless steel.

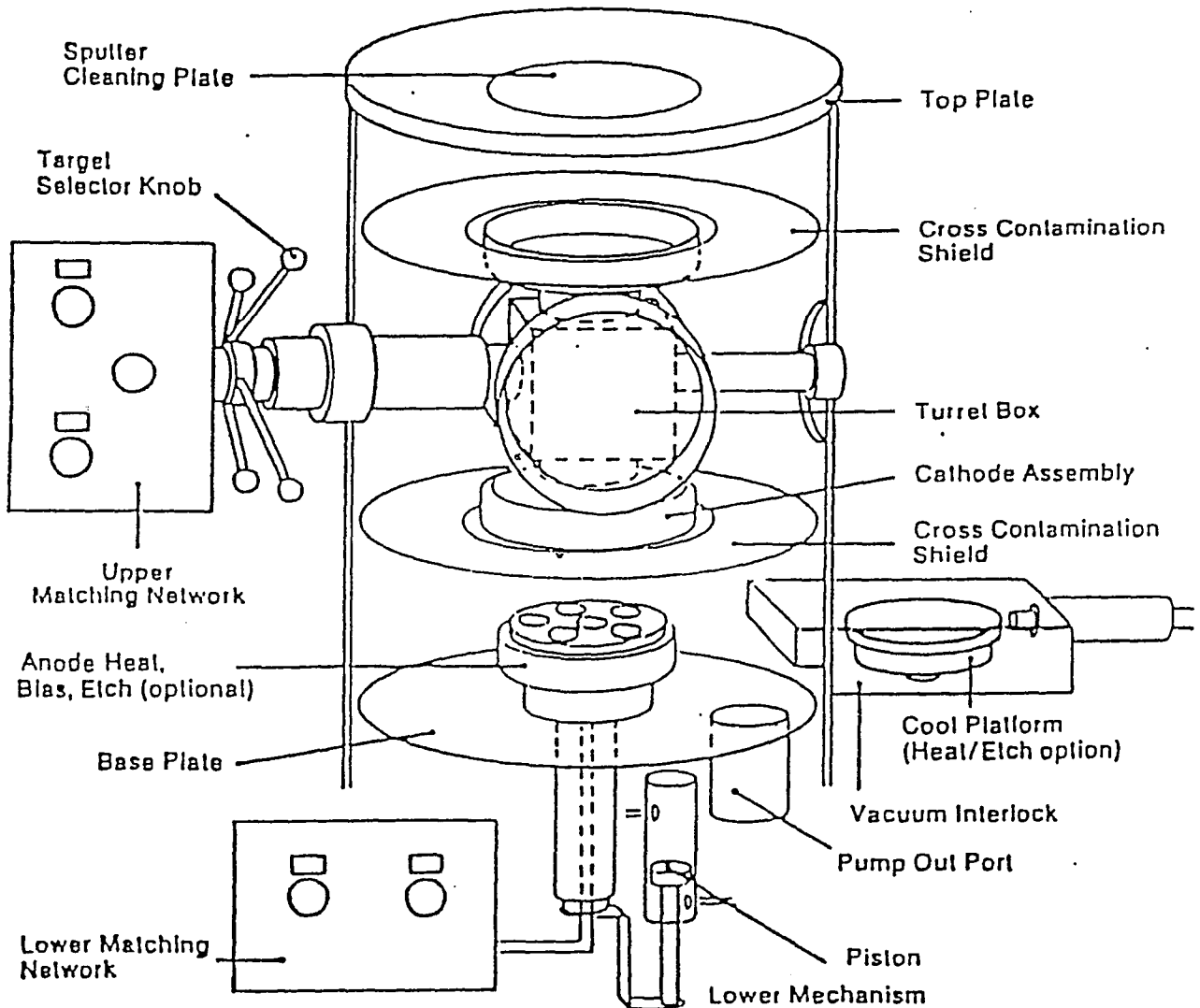


Figure 8. MRC 8800 Sputtering Apparatus.

The desired target could be positioned for sputtering by using the lever on the left hand side in the Fig.8. The gases used for sputtering are supplied to the system through gas cylinders via a micrometering valve provided on the system. The most important parameter of the sputtering process is the vacuum pressure. To consider the vacuum low enough for sputtering, vacuum pressure has to be below  $10^{-6}$  range.

The sputtering system has an intervac chamber. It is connected to the main chamber by a hinged-aluminum door. The samples are first placed in the intervac chamber. The intervac chamber is then pumped down to approximately 10 mtorr. The samples are then transported into the main chamber with a plunger. Thus the vacuum in the main chamber can be preserved.

### 4-3. Substrate preparation

#### 4-3-1. SUBSTRATE

MgO (100) Wafers were used as the substrate for the deposition of thin films of Y-Ba-Cu-O. The advantages of MgO as a substrate for the experiments of this thesis were its lattice constant which is close to that of Y-Ba-Cu-O system and its noninterdiffusive property with deposited film at a relatively high temperature.

#### 4-3-2. SUBSTRATE CLEANING.

- 1). Trichloroethylene bath for 10 minutes.
- 2). Ultrasonic clean in Trichloroethylene for 10 minutes.
- 3). Rinse in Trichloroethylene.
- 4). Transport substrates to intervac immediately after blowing dry the samples with dry Ar.

#### 4-4. Deposition process

The quality of films can be improved by reducing the contamination and improving the base vacuum pressure. To reduce the contamination, the vacuum chamber should be thoroughly cleaned. Since the vacuum chamber wall absorbs moisture from the atmosphere, it is desired that the chamber should not be opened and/or left open for longer durations than necessary.

To run the system, the vacuum of main chamber should be  $10^{-6}$  torr. After the vacuum reaches the above range, the substrates were laid on the platen in the intervac chamber. The intervac chamber was then pumped down to approximately 10 mtorr. The substrate arrangement was drawn in the laboratory notebook for later reference during this pumped down duration.

##### 4-4-1. DEPOSITION PROCESS AT COOLED SUBSTRATE

##### & FOLLOWING POST-ANNEALING PROCESS.

##### A). Deposition process

The sequence of operation is described below:



- 1). The anode was lowered and the desired target is positioned to be sputtered.
- 2). The intervac door was opened and the plunger is moved in.
- 3). The anode was then raised to its upper limit when the plunger is all the way in.
- 4). The plunger is then retracted.
- 5). The anode height is finally adjusted as desired.

After careful insertion of the substrates and the anode height adjustment, the chamber was evacuated for at least 2-3 hours before proceeding to actual deposition. The first step to actual deposition is admitting Ar to the main chamber up to a desired pressure. Initially only Ar was admitted to the chamber for initiating the plasma. Once the plasma was initiated, oxygen gas was introduced to the chamber up to a desired pressure very slowly. RF power was then adjusted to get the desired forward power. The reflected power should not exceed 75 watts, because high reflected power could cause damages to the Rf generator.

The matching network for the target was then tuned to obtain maximum forward power and minimum reflected power. After achieving the best tuning, all the parameters were precisely adjusted to the desired values with only slight adjustments required in tuning. With the steady Plasma, deposition was carried out for the desired length of time and the sputtering parameters were noted.

The deposition parameters for a typical sputtering run were: Base

pressure,  $10^{-6}$  torr; total deposition pressure, 10-30 mtorr (10%  $O_2$ ), anode to cathode distance, 1.8-3.6 inch; forward power, 125 watts; reverse power, 0-6 watts; cathode voltage, 1.6 kilo volts; anode voltage, 0 volts; and target power density  $4.87 \text{ watts/cm}^2$  (target diameter, 2.25 inch).

#### B). Post-deposition annealing process.

The as-deposited films were amorphous from X-ray diffraction analysis, and were generally insulating with room temperature resistances on the order of several megohms. Post-deposition oxygen annealing treatments at temperature above  $800^\circ\text{C}$  are necessary to transform the films to become superconducting at low temperature. The post-deposition annealing was carried out under the following conditions: oxygen pressure  $> 100 \text{ Torr}$ ; temperature ,  $670^\circ\text{C} - 830^\circ\text{C}$  for (10 min); warming rate ,  $2.3^\circ\text{C/min}$ ; cooling rate ,  $5^\circ\text{C/min}$ .

#### 4-4-2. DEPOSITION PROCESS AT THE CRYSTALLIZATION TEMPERATURE.

The sequence of operation is described below:

- 1). The platen was positioned on the anode by the plunger.
- 2). The chamber was opened and the substrate heater was installed on the platen.
- 3). The anode height was adjusted as desired.
- 4). The substrates and thermocouple were positioned on the substrate holder.

- 5). The chamber was closed and pumped down to  $10^{-6}$  Torr.
- 6). The substrate holder was heated up to the crystallization temperature.

The deposition parameters for these runs were: background pressure,  $10^{-6}$  Torr; total pressure, 10 - 35 mTorr (10%  $O_2$ ); anode to cathode distance, 1.8 - 3.6 inch; forward power, 90 - 125 Watts; reverse power, 0 - 10 Watts; cathode voltage, 1.3 - 1.6 Kvolts; anode voltage, 0 volts; substrate temperature, 500 - 715°C.

#### 4-5. Heater & substrate holder preparation for high temperature deposition process.

The substrate holder was made of Haynes alloy 230. Most of the other metals would be oxidized at high temperature (500-700°C) under oxygen atmosphere even stainless steel. The Haynes alloy 230 neither oxidized nor wrenched under these conditions. Because of these properties, Haynes alloy 230 was selected as a substrate holder for high temperature deposition process.

Nichrom wire was used as heat element for the substrate heater. The substrate temperature was measured with a chromel alumel thermocouple near the center of substrate holder.

#### 4-6. Four-probe contact preparation

As shown in fig.9, four silver dots were deposited on the film to make ohmic contact and easier indium soldering. The connection between measurement system and film was carried out by four silver layer deposited on the glass.

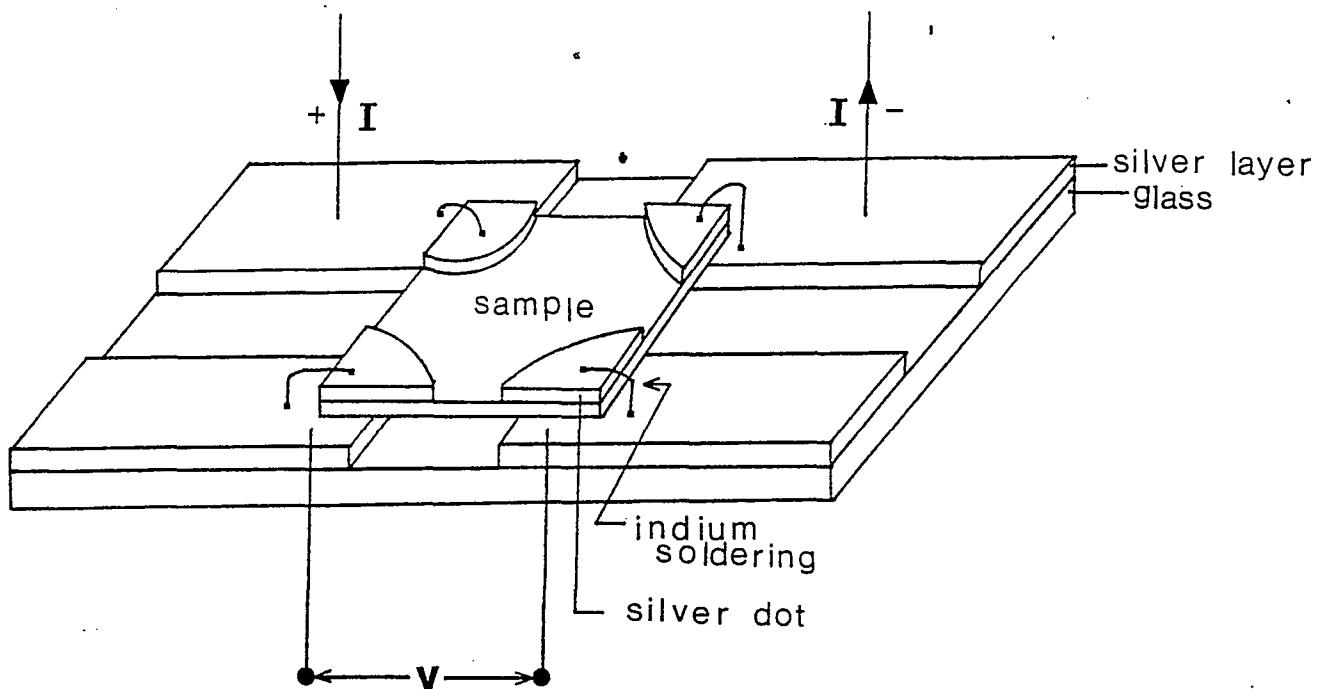


Figure 9. Four-point probe contact by indium soldering on silver dots.

## 5. EXPERIMENTAL RESULTS AND DISCUSSION

### 5-1. Introduction.

Deposition conditions affect the film properties significantly and these properties can be varied in a controlled manner by controlling the deposition parameters. Temperature dependence of electrical resistance of reactively sputtered Y-Ba-Cu-O superconducting films were studied as a function of the substrate temperature  $T_s$  and post-deposition annealing condition. The variation of film composition and thickness or deposition rate as a function of radial deposition position, gas pressure, target distance and  $T_s$  was investigated. The effect of  $T_s$  on the film resistance at room temperature was studied.

The experiments concentrated on finding the optimum preparation condition for obtaining high quality thin Y-Ba-Cu-O superconducting films for the future work in Drexler Microelectronics Laboratory.

### 5-2. Substrate Temperature Effect.

There have been many efforts to grow high quality thin films of superconducting oxides for technological applications.<sup>(12,13)</sup> For application to electronic devices, a low temperature deposition process controlling the crystalline state and electric property is essential. In view of this aspect, Y-Ba-Cu-O thin films were prepared

at 500°C to 715°C. The relation between  $T_g$  and superconducting properties, deviation from the stoichiometric composition and film thickness was studied.

#### 5-2-1. EFFECT OF SUBSTRATE TEMPERATURE ON THE FILM COMPOSITION AND DEPOSITION RATE.

Fig.10 depicts the dependence of deposition rate on the substrate temperature. With increase in substrate temperature from 500°C to 715°C, the deposition rate decreased from 35 A/min. to 8 A/min. It can be seen that the deposition rate is inversely proportional to the substrate temperature. This is explained by the variation in sticking coefficient which is also inversely proportional to the substrate temperature.

The dependence of the composition of the films on substrate temperature  $T_g$  is also shown in Fig.10. If we increase the target distance from 2 inches to 2.5 inches then the composition ratio of Cu and Ba of the films deposited at substrate temperature of 650°C may be changed higher than that of figure 10. It was found that the films sputtered at 500°C have stoichiometric composition, while the films sputtered at 650°C to 715°C were non-stoichiometric. The RBS data of these films shown in appendix B.

The following sputtering parameters were used for this experiment.

Table 1

Sample Number	<sup>1</sup> Total Gas Pressure (mtorr)	Target Distance (inches)	Forward Power (watts)	Radial Position (inches)	Substrate Temperature	Radial Angle (Y:Ba:Cu)	Ratio of (Y:Ba:Cu)	Film Thickness (angstroms)
Qy33S4	35	2.5	100	2	500°C	24.2°	1:2:3	8400
Qy34S2	35	2.0	100	2	650°C	29.4°	1:1.3:2	3800
Qy36S2	35	2.5	100	2	715°C	24.2°	1:1.4:2.5	1920

<sup>1</sup> The total sputtering gas pressure consists of 90% Argon gas and 10% Oxygen gas.

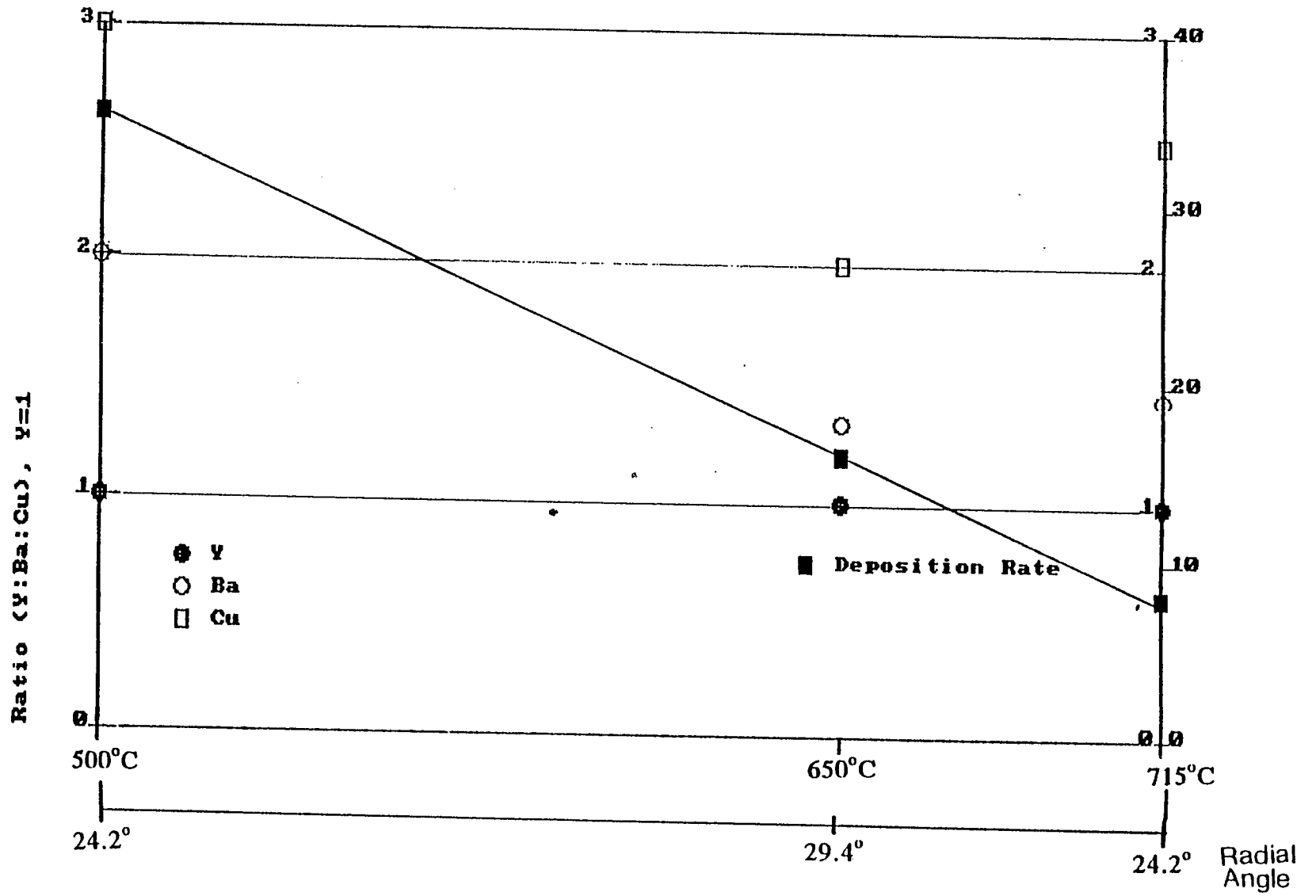


Figure 10, The variation of deposition rate and film composition as a function of the substrate temperature.



## 5-2-2. EFFECT OF SUBSTRATE TEMPERATURE ON THE TEMPERATURE DEPENDENCE OF ELECTRICAL RESISTANCE.

Fig.11 shows the temperature dependence of electrical resistance of as-grown films prepared at various substrate temperatures: (a)  $T_s$ , 500°C, (b) 650°C, (c) 715°C. The resistance of as-grown films prepared at a substrate temperature of 715°C is 4 ohms at 300°K, as shown in Fig.12. As the substrate temperature decreases, the resistance changes in accordance with the increase in the resistance at room temperature. It was found that for all as-grown films the temperature dependence of resistance in the normal state is semiconductive. This can be explained by the composition deviation which caused by high substrate temperature. As-grown films deposited at substrate temperature from 650°C to 710°C have  $T_{co}$  (onset transition temperature) of about 85°K and  $T_{ce}$  (endpoint transition temperature) of about 25°K. The films prepared at substrate temperature at 500°C have  $T_{co}$  of 10°K. We were not able to measure  $T_{ce}$  due to the instrument limitation.

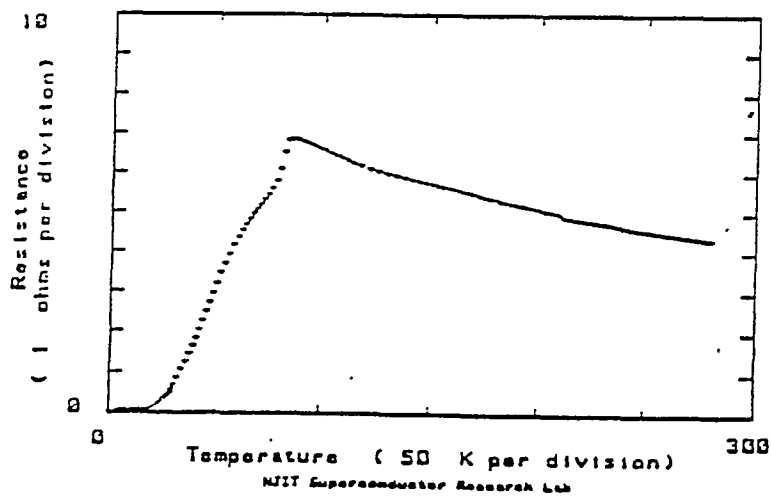
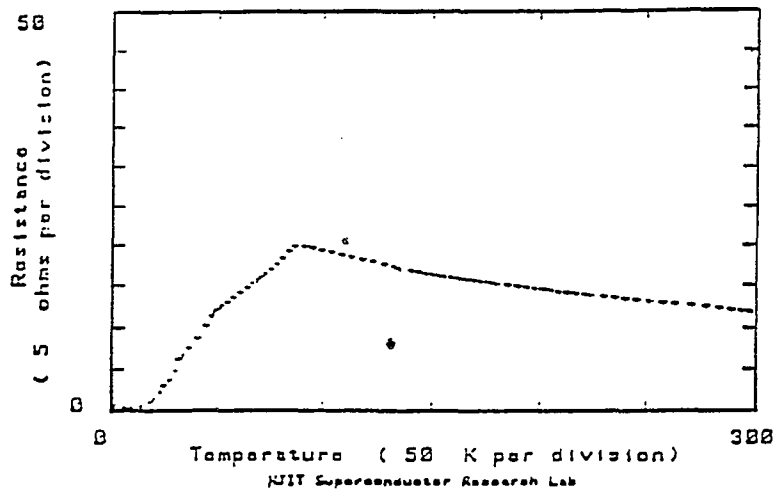
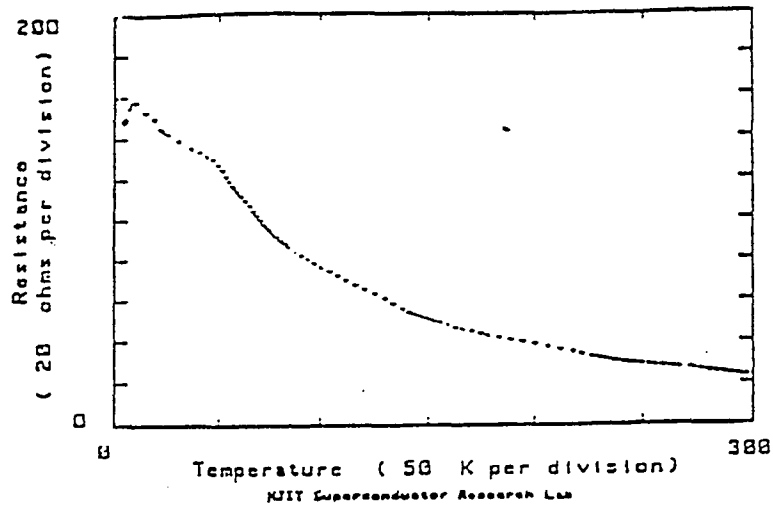


Figure 11. Temperature dependence of electrical resistance for as-grown films prepared at, (a)  $500^{\circ}\text{C}$  (b)  $650^{\circ}\text{C}$  (c)  $715^{\circ}\text{C}$ .

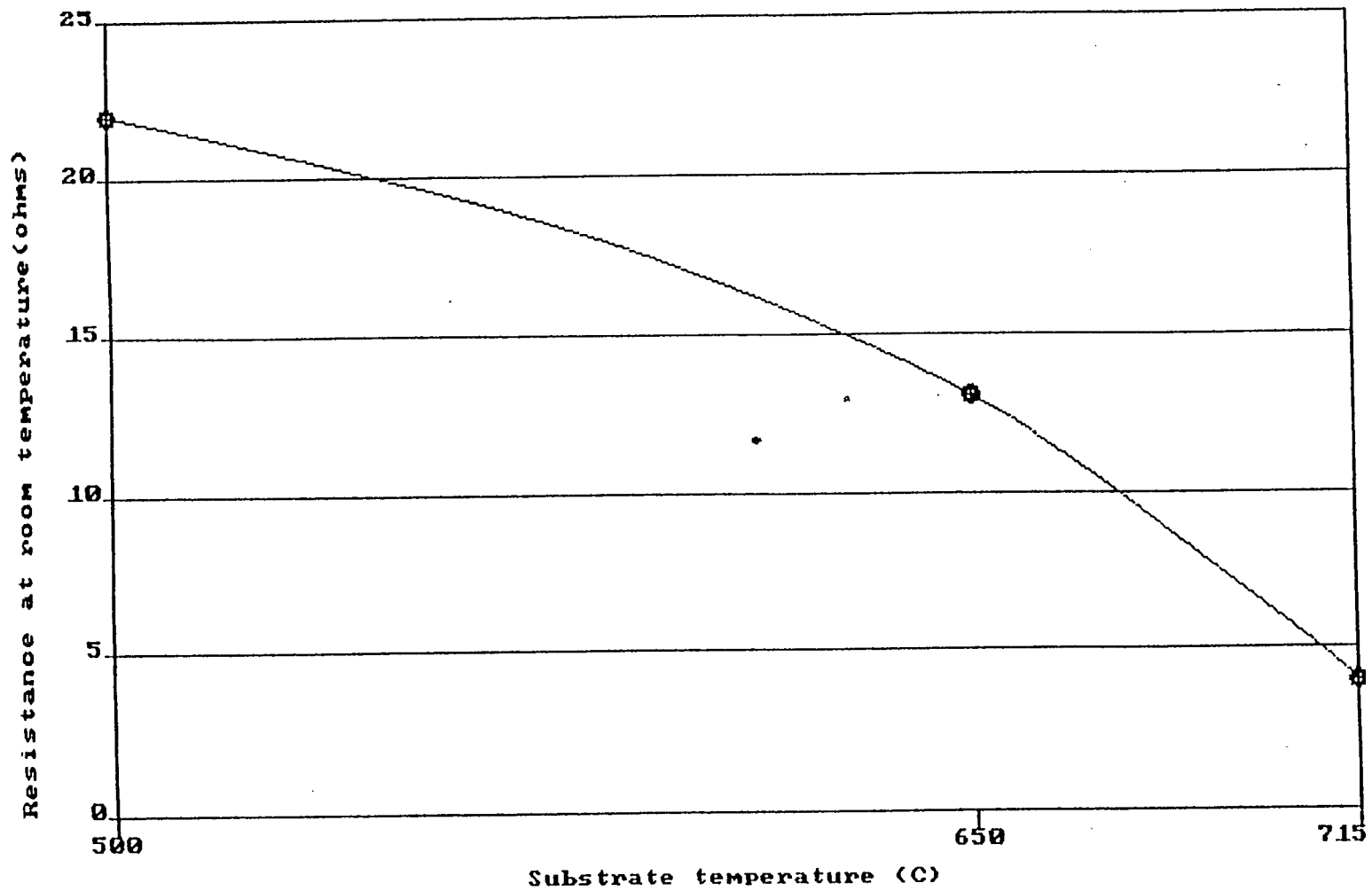


Figure 12, The variation of resistance at room temperature as a function of substrate temperature.

### 5-3. Effect of radial angle and resputtering on the film composition and thickness.

The compositions, as a function of radial distance under the target, were determined for the films prepared at several radial distance. As shown in fig.13, the sputtering gas for the run 39 was a 9:1 mixture of Ar and O<sub>2</sub> at the pressure of 10 mTorr. An forward power of 125 w provided and the distance between target and substrate holder was 2.5 inches. The variation of the film composition and thickness as a function of radial distance is shown in fig.14, where the film directly under the target was completely resputtered, with the substrate also eroded. As the resputtering effect decreases beyond the edge of the target, film composition approaches that of the bulk target. The desired Y:Ba:Cu ratio of 1:2:3 was obtained at the radial angle between 33° and 40.4°. Film loss during sputtering from a Y<sub>2</sub>O<sub>3</sub> target has been reported by Hanak and Pellicane<sup>14</sup>, while Shintani<sup>15</sup> et al. observed intense substrate heating and film loss when sputtering from a BaTiO<sub>3</sub> target, Shintani attributed erosion in the case of BaTiO<sub>3</sub> to a high measured yield of energetic sputtered neutrals. The same phenomenon may also be applicable to Y-Ba-Cu-O resputtering.

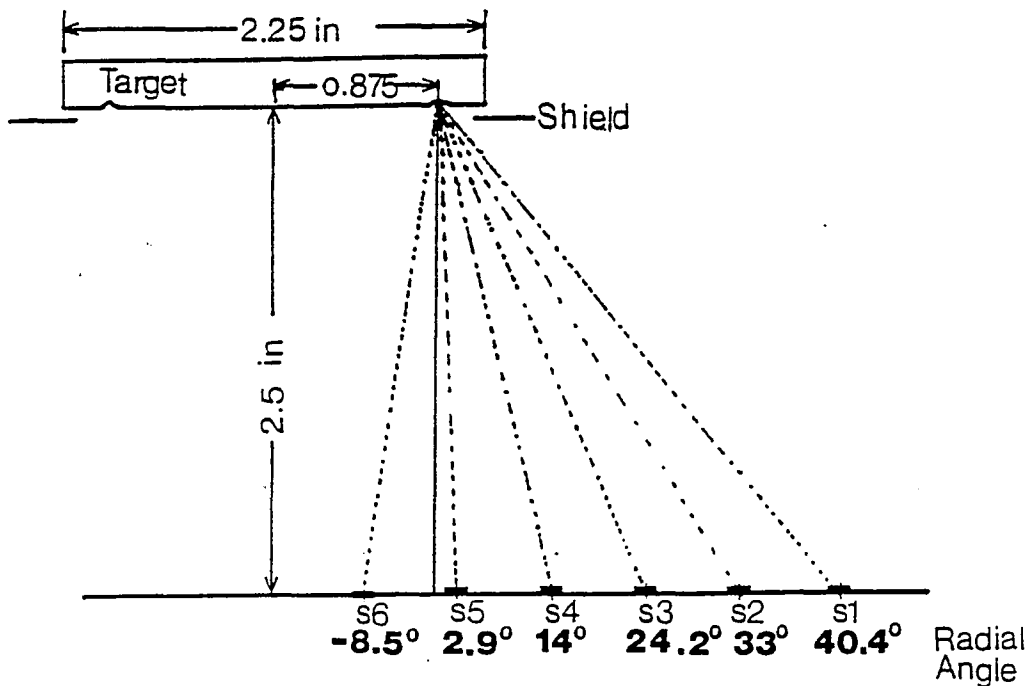
Oxygen anion can also cause resputtering. O<sup>-</sup> and O<sup>-2</sup> anions have been known to form during sputtering<sup>16</sup> and then accelerated to the substrate across the applied electric field. Thus we can presume, the resputtering may be due to energetic neutral particle bombardment and/or negative ion bombardment. The etching phenomenon occurred in a

sharply defined region which closely matched the size and shape of the ground shield opening of the target. This may be unique method of thin film processing. For example, a pattern can be made on films by placing the samples to be patterned in the etching region. This method allows etching without contamination, due to the fact that the etching particles and films are the same material.

It was also observed that the deposition rate depends very strongly on the radial angle. As might have been expected in the cosine law\* of emission, the film thickness is inversely proportional to the distance between target and substrate, when the angle exceeds  $14^\circ$ .

The temperature of substrate was measured during film deposition. The substrate temperature  $T_s$  was in the order of  $130^\circ\text{C}$ . The substrate heating can be caused by the following sources of energy<sup>17</sup>: (1) radiation from the plasma, (2) kinetic energy of argon ions, electrons and gaseous neutrals, (3) release of latent heat by atoms deposited on the substrate, and (4) kinetic energy of atoms deposited on the substrate. The substrate heating during rf diode sputtering with Y-Ba-Cu-O target has been reported by Shah and Carcia. The authors attributed the substrate heating to secondary electrons emitted during the sputtering process from the Y-Ba-Cu-O target, mostly from Ba and Y. A very high secondary electron yield from Ba and Y during sputtering can be expected since both Y and Ba have very small work functions<sup>19</sup> 3.1eV and 2.7eV respectively.

\* See Appendix A



\*Films deposited at several radial angles with fixed target distance.

Table 2

Sample #	<sup>2</sup> Total Gas Pressure (mtorr)	Total Target Distance (inches)	Forward Power (watts)	Radial Position (inches)	Substrate Temperature	Radial Angle	Ratio of Thickness (Y:Ba:Cu)	Film Thickness (Angstroms)
Qy39S1	10	2.5	125	3.0	130°C	40.4°	1:2:3	2100
Qy39S2	10	2.5	125	2.5	130°C	33.0°	1:2:3	4500
Qy39S3	10	2.5	125	2.0	130°C	24.2°	1:2.1:3	5700
Qy39S4	10	2.5	125	1.5	130°C	14.0°	1:2:3	6600
Qy39S5	10	2.5	125	1.0	130°C	2.9°	1:0.7:2.8	5100
Qy39S6	10	2.5	125	0.5	130°C	-8.5°		

Figure 13. Deposition map and sputtering condition of the run Qy39

<sup>2</sup>See the footnote of page 46

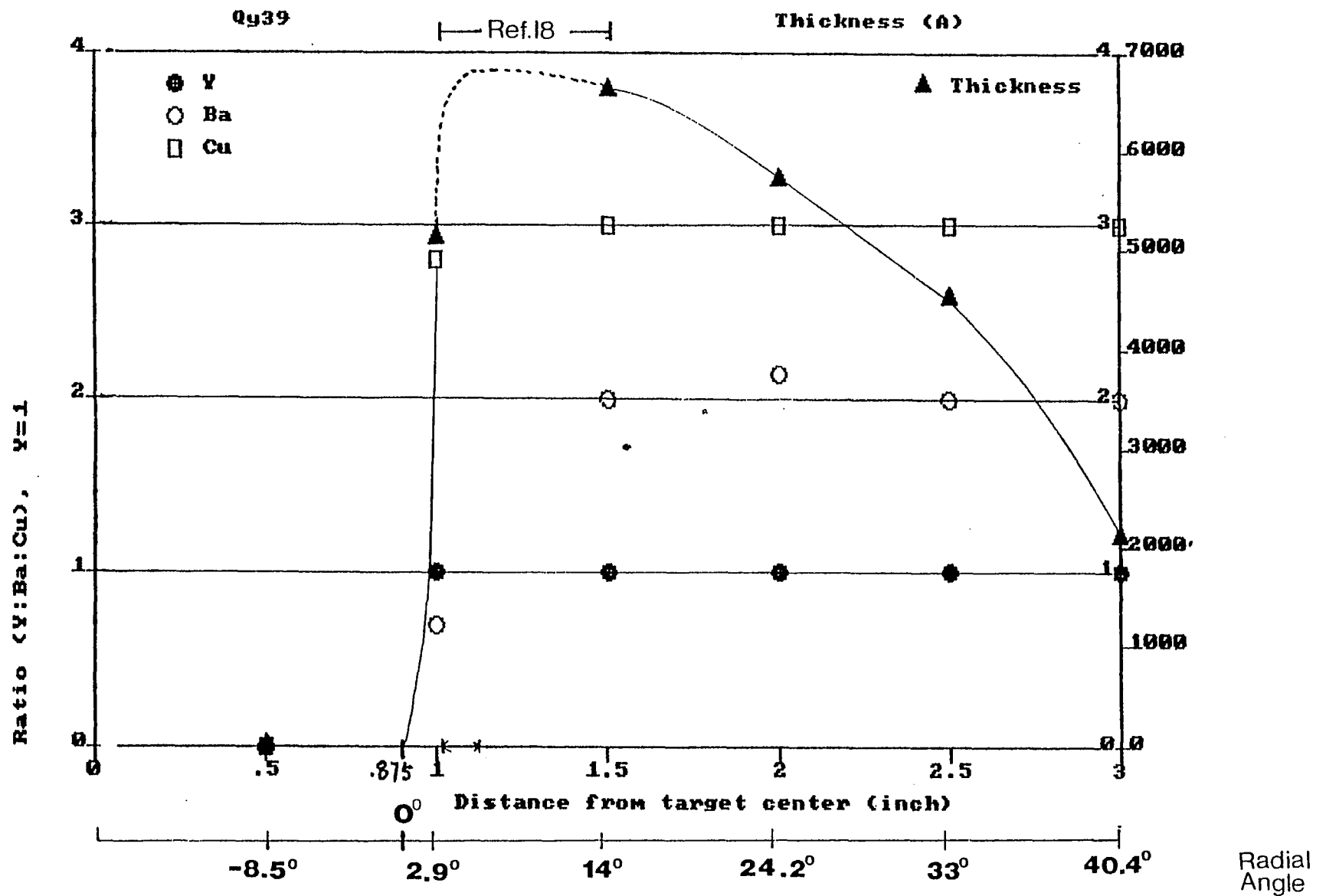


Figure 14, The variation of film composition and thickness as a function of radial angle.

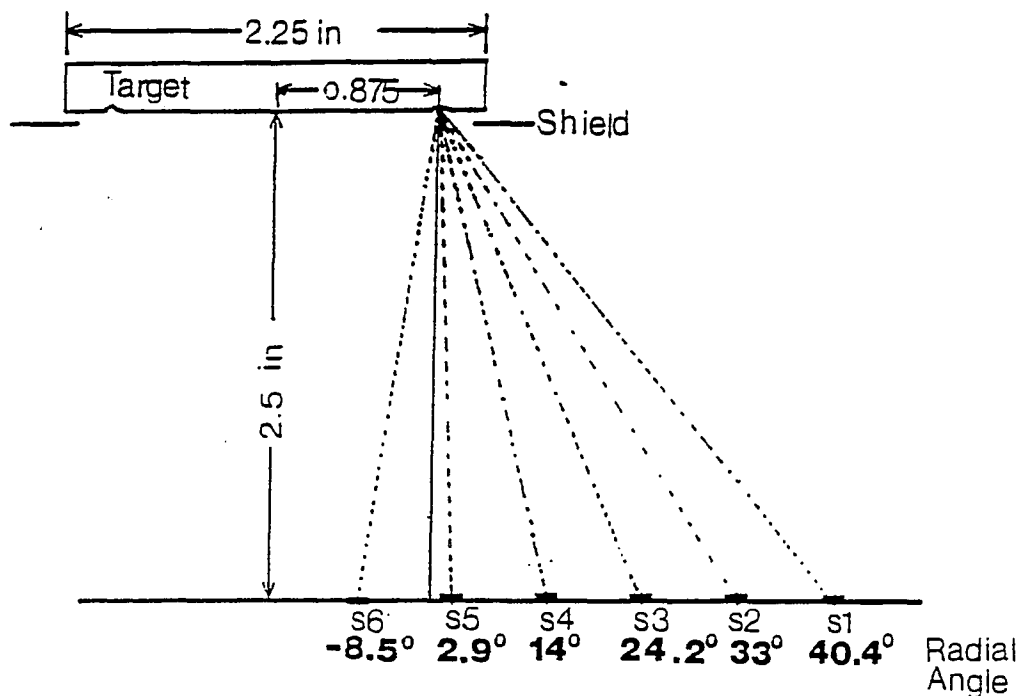


Table 3

Sample #	<sup>3</sup> Total Gas Pressure (mtorr)	Target Distance (inches)	Forward Power (watts)	Radial Position (inches)	Substrate Temperature (°C)	Radial Angle	Ratio (Y:Ba:Cu)	Film of thickness (Angstroms)
Qy40S1	10	2.5	125	3.0	130°C	40.4°	1:2:3	2350
Qy40S2	10	2.5	125	2.5	130°C	33.0°	1:2:3	3600
Qy40S3	10	2.5	125	2.0	130°C	24.2°	1:2.2:3	5520
Qy40S4	10	2.5	125	1.5	130°C	14.0°	1:1.8:3	6600
Qy40S5	10	2.5	125	1.0	130°C	2.9°	1:7:2.8	5400
Qy40S6	10	2.5	125	0.5	130°C	-8.5°		

Figure.15 Deposition map and sputtering condition of the run Qy40

<sup>3</sup>See the footnote of page 46.



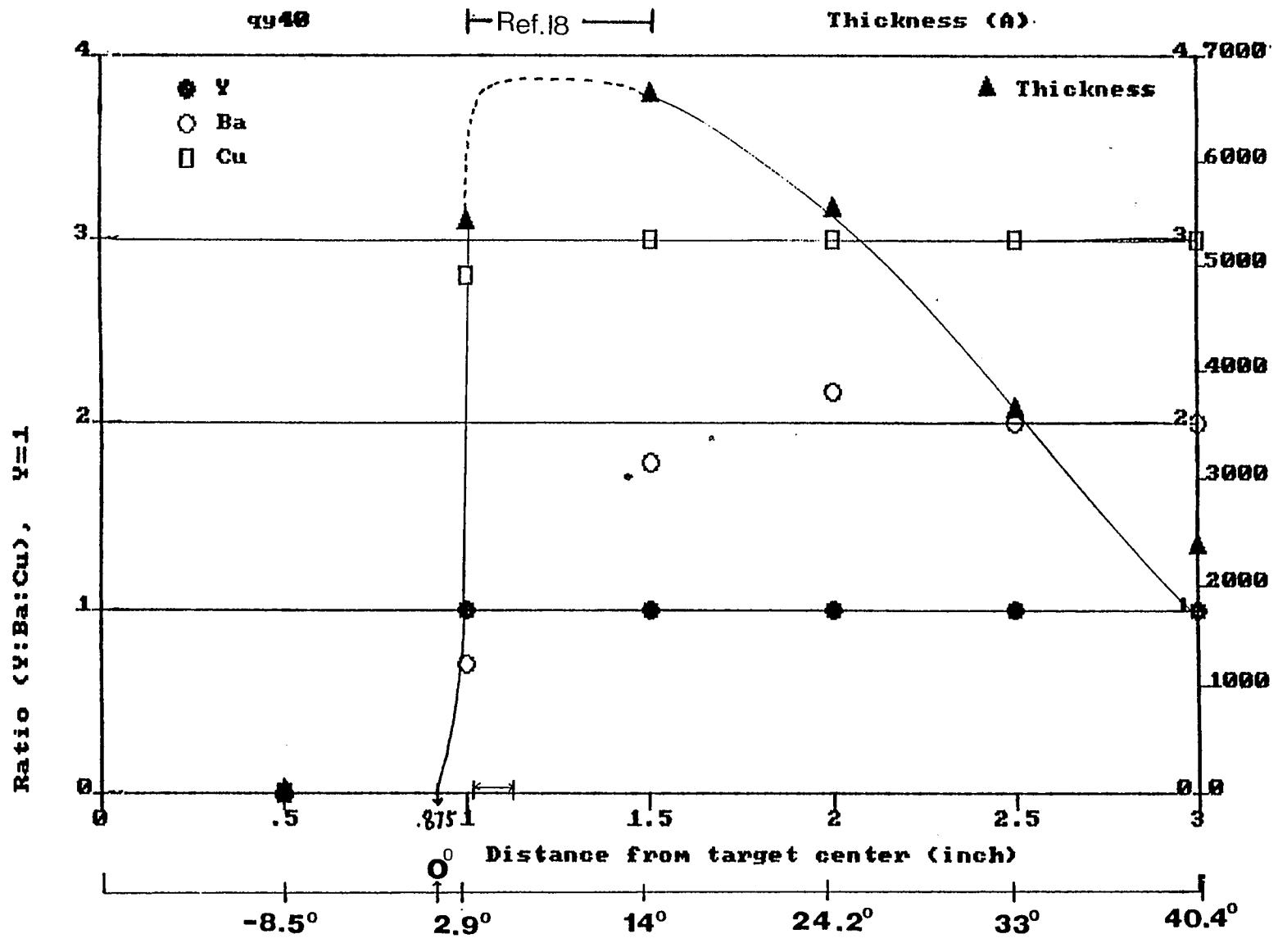


Figure 16, The variation of film composition and thickness as a function of radial angle.

#### 5-4. Effect of gas pressure on the film composition and thickness.

Fig.17 shows the variation of film composition and thickness for films prepared at various gas pressure, with fixed oxygen partial pressure (10%). The film deposition condition of this experiment described in table 4. The increase of the total gas pressure resulted in significant deficiency of Ba elements. RBS data for the films prepared for this experiment shown in Appendix E.

Table 4

Sample #	<sup>4</sup> Total Gas Pressure (mtorr)	Target Distance (inches)	Forward Power (watts)	Radial Position (inches)	Substrate Temperature	Radial Angle	Ratio of (Y:Ba:Cu)	Film Thickness (Angstroms)
Qy39S3	10	2.5	125	2.0	130°C	24.2°	1:2.14:3	5700
Qy41S8	20	2.5	125	2.0	130°C	24.2°	1:1.2:3	9600
Qy42S7	30	2.5	125	2.0	130°C	24.2°	1:1.2:3	7200

<sup>4</sup>See the footnote of page 46.

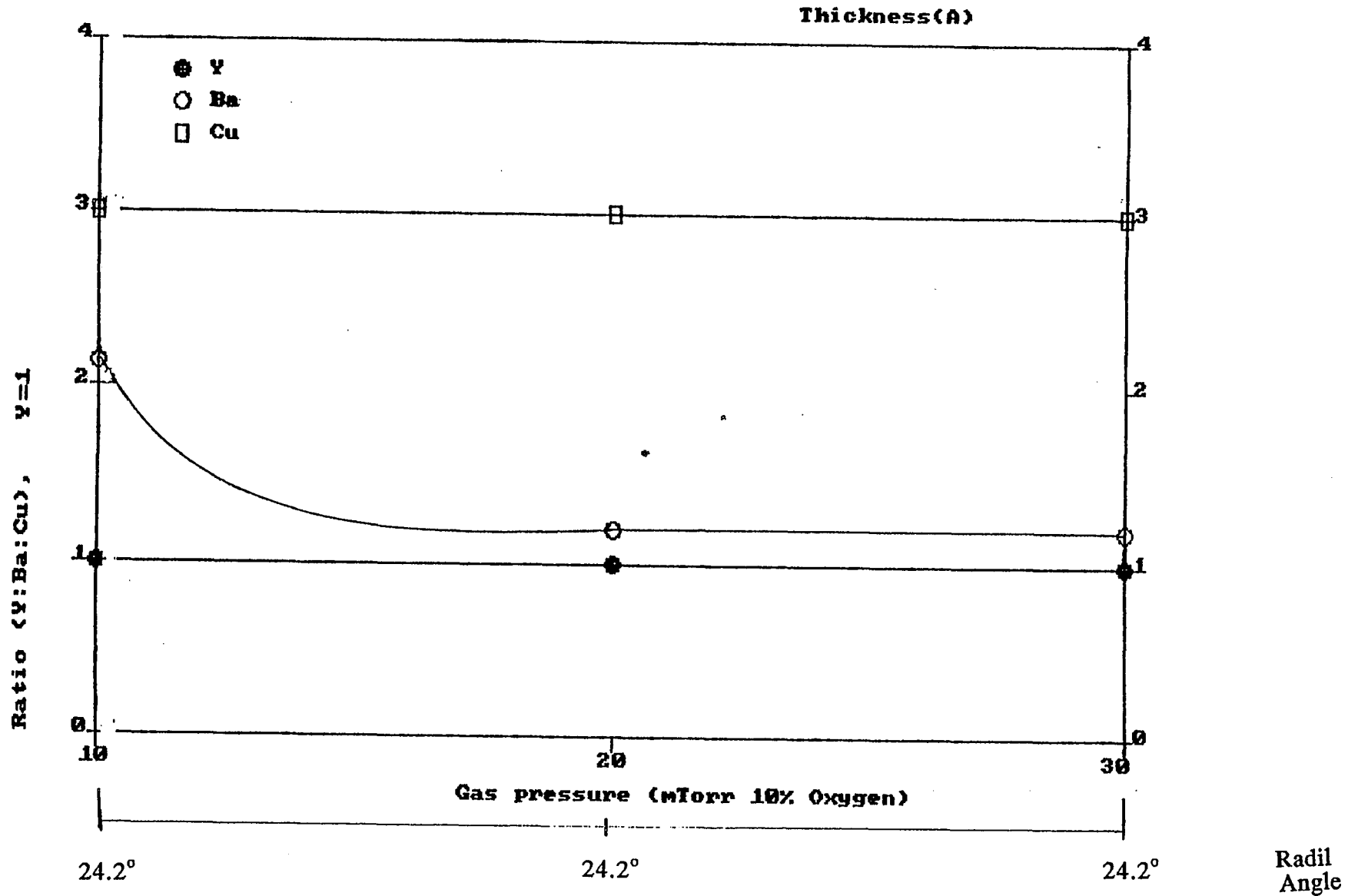


Figure 17, The variation of film composition and thickness as a function of sputtering gas pressure.

## 5-5. Effect of target distance on the film composition and thickness.

The dependence of distance between target and substrate on the film composition and thickness is shown in Fig.19. It was observed that for the distance of 1.8 inch, the ratio of Ba/Y was 1, and with a increasing target distance to 3.6 inches, the ratio of Ba/Y increased to 2.45.

Ba deficiency in the films which were deposited by rf diode sputtering was reported by Gilbert et al<sup>(20)</sup> and Shah and Carcia<sup>(21)</sup>. They attributed it to preferential resputtering of Ba from the film or to the substoichiometric sputtering due to formation of Ba<sup>+</sup> ions. These ions were believed to be recaptured by the cathode causing the film to be Ba deficient. In addition, since the substrate temperature is high (130°C) under rf diode deposition conditions<sup>17</sup>, an evaporation of the Ba atoms is also probable.

The sputtering condition is shown in table 5 and the deposition schematic arrangement is shown in figure18. The corresponding RBS data of these films included in Appendix F.

Table 5

Sample #	Total Gas Pressure (mtorr)	Target Distance (inches)	Forward Power (watts)	Radial Position (inches)	Substrate Temperature	Radial Angle	Ratio of (Y:Ba:Cu)	Film Thickness
Qy43S8	10	1.8	125	2.0	130°C	32.0°	1:1:3	4200
Qy39S3	10	2.5	125	2.0	130°C	24.2°	1:2.14:3	5700
Qy44S8	10	3.6	125	2.0	130°C	17.4°	1:2.5:3.75	11700

<sup>5</sup>See the footnote of page 46.

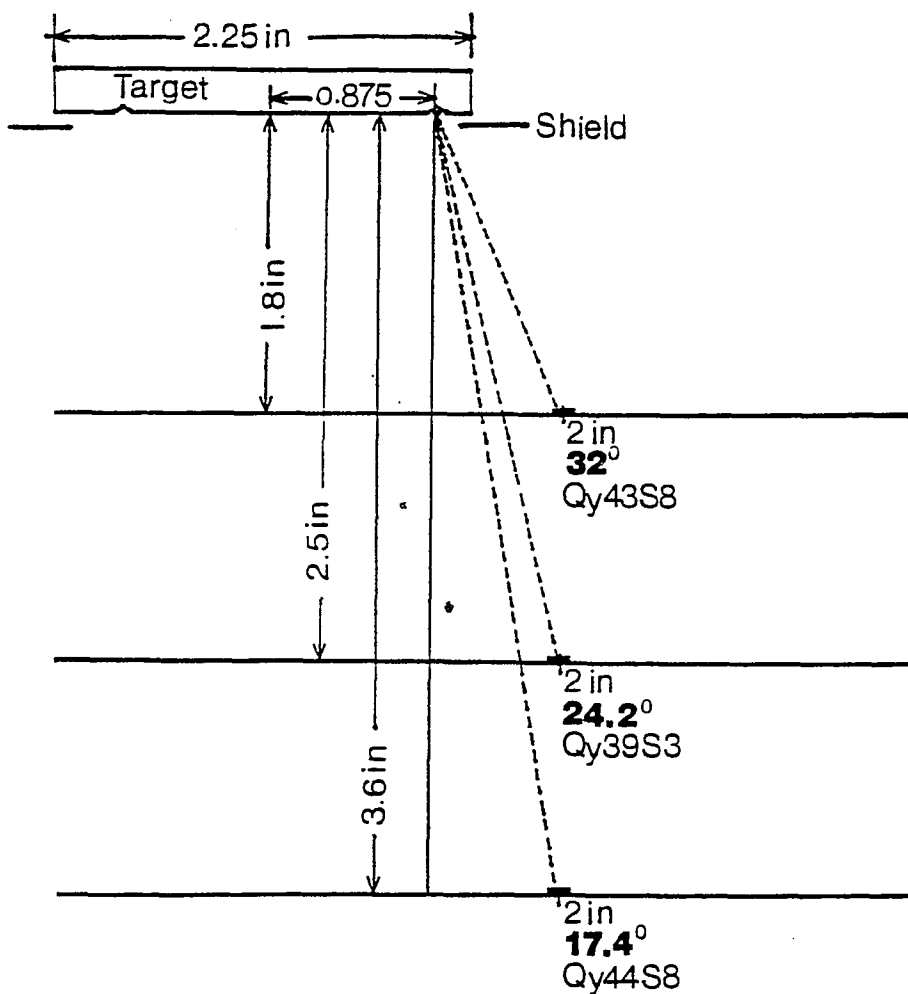


Figure 18. The films deposited under three different target distance with fixed radil position.

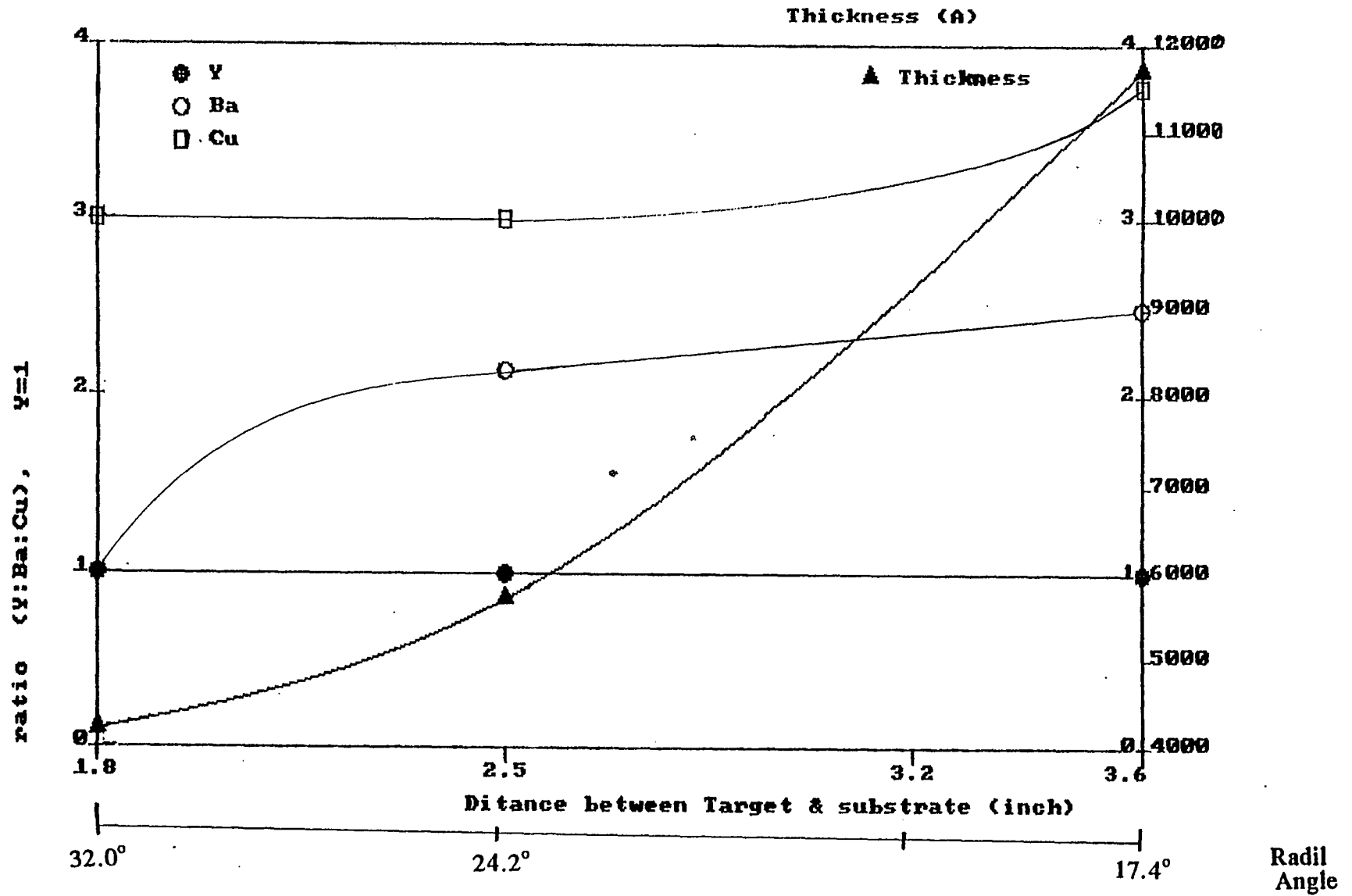


Figure 19 The variation of film composition and thickness as a function of the distance between target and substrate.

## 5-6. Annealing effect on the temperature dependence of electrical resistance.

Fig.20 shows the temperature dependence of electrical resistance for the films prepared on cooled substrates with post-deposition annealed at 820°C for 10 minutes and 670°C for 10 min. All of the as-grown films were found to be insulating and amorphous with room temperature resistances ranging in the order of several megaohms. The post annealing changes the room temperature resistances in the range of 0.5 to 1.8 ohms.

The films with post annealed at 820°C for 10 minutes, have  $T_{co}$  of about 70°K and  $T_{ce}$  of about 50°K. The temperature dependence of resistance in the normal state is metallic.



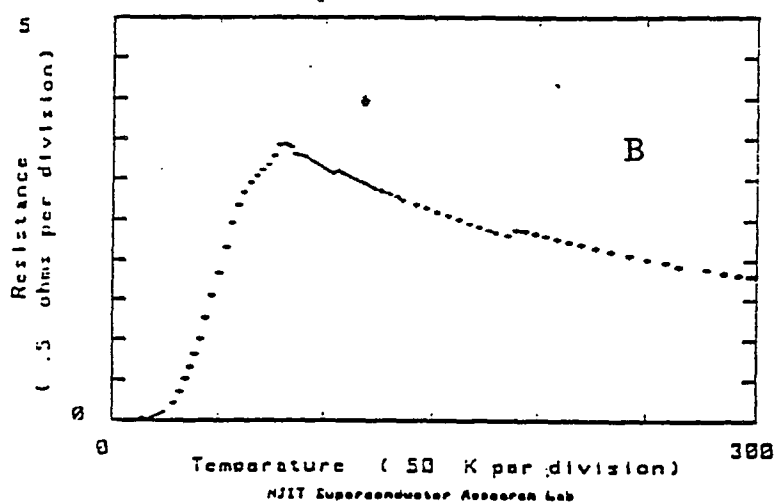
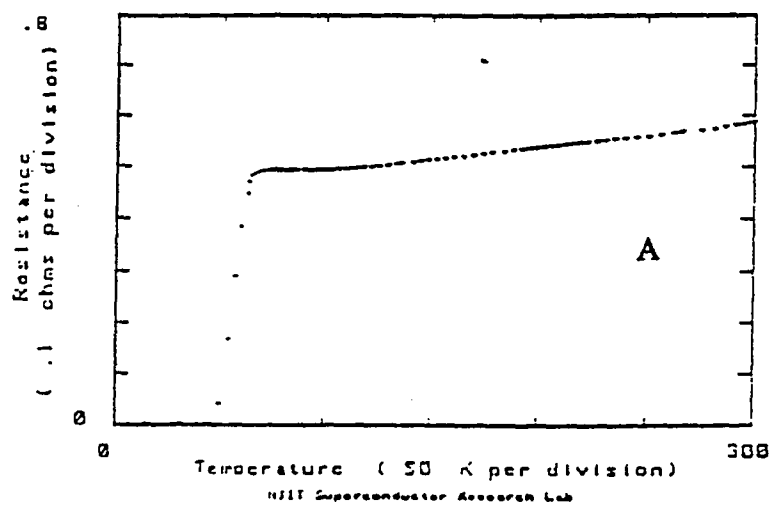


Figure 20 The temperature dependence of electrical resistance for the films prepared on cooled substrate with post-deposition annealed at (a)820°C for 10 min, (b)670°C for 10 min.

## 6. CONCLUSIONS AND SUGGESTIONS FOR FUTURE WORK.

### 6-1. Conclusions.

In summary, the stoichiometric  $\text{YBa}_2\text{Cu}_3\text{O}_{7-x}$  films were successfully grown on MgO (100) substrates from a single sintered  $\text{YBa}_2\text{Cu}_3\text{O}_x$  target by rf diode sputtering, under the condition of; substrate temperature, 130°C-500°C; total gas pressure, 10 mTorr; radial position of substrate, 2.5 inches; target distance, 2.5 inches; forward power, 125 W; target power density, 4.87 watts/cm<sup>2</sup>; deposition time, 4 hours.

Substrate heating and resputtering were observed during the deposition by rf diode sputtering. The rise in substrate temperature may be due to secondary electron bombardment. Lau et al<sup>(17)</sup> have shown that secondary electron bombardment is the main cause of substrate heating. Resputtering may be mostly due to energetic neutral particles<sup>(15,21)</sup> and Oxygen anions bombardment<sup>(16,22)</sup>

Thin Y-Ba-Cu-O superconducting films were grown by two different processes : (1) deposition at a low substrate temperature followed by a post-deposition annealing at around 830°C for 10 minutes ; (2) deposition at the crystallization temperature under oxidizing atmosphere. For the process (1) high temperature post-deposition annealing has been necessary.<sup>(23)</sup> The high temperature treatment causes; poor surface morphology, cracking, or undesirable

interdiffusion, This limits the choice of substrate materials.<sup>(24,25)</sup> To overcome difficulties associated with high temperature process the second process is preferred. From the RBS measurement, it was also found that the Cu and Ba contents in the films decreased with increasing substrate temperature. Thus the preferred way to fabricate reasonably high quality thin superconducting  $\text{YBa}_2\text{Cu}_3\text{O}_{7-x}$  films with our sputtering system is the second process technique using target with Cu and Ba contents increased.

## 6-2. Suggestions for future work.

The following suggestions for future Y-Ba-Cu-O superconducting thin film research are suggested by this author :

- (1) The bombardment of the secondary electrons and negative ions to the growing surface could be eliminated by applying a transverse magnetic field.
- (2) The nonstoichiometry composition of deposited films when deposition is made at the crystallization temperature of substrate can be corrected by the use of a target increased with Cu and Ba.
- (3) The effect of substrate bias on the film composition should be studied.
- (4) Resputtering etching resin may be used to make a pattern on the thin films. this method allows etching without contamination, due to the fact that the etching particles and

films are the same material.

- (5) A high total gas pressure and low forward power could be helpful for reducing the resputtering. Since the mean free path of  $\text{Ar}^+$  will be reduced under high Ar gas pressure the energy of ejected neutral particles will also be reduced and the low forward power will reduce the bombardment flux of negative particles to the growing surface.

## REFERENCE

- 1). Physica C 153-155 (1988) 3-8.
- 2). Appl. Phys. Lett. 54 (17), 24 1989.
- 3). Rev. Mod. Phys. 61 No2 1989.
- 4). Jap. J. of Appl. Phys. Vol 26 No5 May 1987 L791-793.
- 5). Jap. J. of Appl. Phys. Vol 26 N011 Nov. 1987 L1907-1909.
- 6). Jap. J. of Appl. Phys. Vol 26 No9 sep. 1987 L1561-1568.
- 7). J.M Wall, Methods of surface analysis. Cambridge univ. Press.
- 8). Chu, W.K. Mayer, J.W. & Nicolet, M.A. (1978).  
Back Scattering Spectrometry, Academic Press.
- 9). X-ray Diffraction procedures, Harold, P.K. & Leroy, E.A.
- 10). Crystal Structure Analysis, Jenny, P.G. & Kenneth, N.T.
- 11). S.M. Sze, Semiconductor Device, Wily
- 12). Appl. Phys. Lett. 51 1987 200.
- 13). Phys. Rev. B35 1987 8824.
- 14). J.J. Hanak et al. J. Vac. Sci. Tech. 13 406 (1976).
- 15). Y. Shintani et al. Jap. J. Appl. Phys. 14 1875 (1975).
- 16). R.E. Honig. J. Appl. Phys 29 549 (1958).
- 17). S.S. Lau et al. J. Vac. Sci. Tech. 9 1196 (1972).
- 18). H. Kim. Research Seminar Presentation 1989.
- 19). H.B. Michaelson. IBM J. Res. Develop. 22 72 (1978).
- 20). L.R. Gilbert et al. J. Vac. Sci. Tech. 17 389 (1980).
- 21). S.I. Shah, & P.F. Carcia, AIP Conf. Proc. No165, P50-57 1988.

- 22). R.E. Honig. *Advances in Mass Spectroscopy* (pergamon, N>Y> 1962)  
VOL.2 p25.
- 23). J. Kwo, T.C. Hsieh, R.M. Fleming, M. Hong, *Phys. Rev. B* 36 1987  
4039.
- 24). D. Dijkkamp, T. Venkatesan, X. D. Wu, *Appl. Phys. Lett.* 51 619  
1987.
- 25). X.D. Wu, A. Inam, T. Venkatesan, *Appl. Phys. Lett.* 52 1988 754.

## APPENDIX A

### THICKNESS PROFILES RESULTING FROM THE COSINE-SQUARE LAW OF DISTRIBUTION FOR POINT AND CIRCULAR DISK SOURCES<sup>(60)</sup>

According to the cosine-square law\*, emission of material resulting from a small area does not occur uniformly in all directions but favors directions approximately normal to the emitting surface. The amount of material which condenses on an opposing surface depends on the position of the receiving surface with regard to the emission source.

As shown in figure E.1, the material contained in an evaporant beam of solid angle  $d\omega$  covers an area which increases with distance as well as with the angle of incidence  $\theta$ . The element of the receiving surface which corresponds to  $d\omega$  is  $dA_r = r^2 d\omega / \cos\theta$ .

Therefore, the mass deposited per unit area is

$$\frac{dM_r(\phi, \theta)}{dA_r} = \frac{M_\theta \cos\theta \cos\phi}{\pi r^2} \quad (E.1)$$

where  $M_\theta$  is the total mass of evaporated material.

The mass evaporation rate per unit area  $T$ , assuming a uniform evaporation rate across the entire evaporation area, is related to  $M_\theta$  through the double integral

$$M_\theta = \iint_{A_\theta} T dA_\theta dt \quad (E.2)$$

---

\* Cosine-square law of distribution is also applicable to single element sputtering

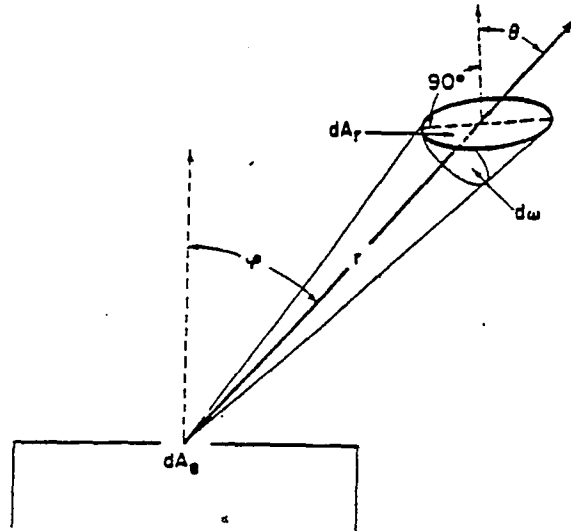


Figure E.1 Surface element  $dA_r$  receiving deposit from a small-area source  $dA_s$

If  $\rho$  is the density of the film material and  $d$  is the thickness of the film, the small mass  $dM_r$  will occupy a volume  $dA_r d$ . The film thickness can be written as

$$d = \frac{dM_r}{\rho dA_r} \quad (E.3)$$

In practice evaporations are performed with sources whose evaporating surfaces are not vanishingly small. The source is assumed to be a circular disk of radius  $s$  emitting toward a plane-parallel receiver. Therefore, the distribution of material on the substrate plane is centrosymmetrical and can be described by one coordinate, the center distance  $l$ . The arrangement is shown schematically in figure E.2. A particular



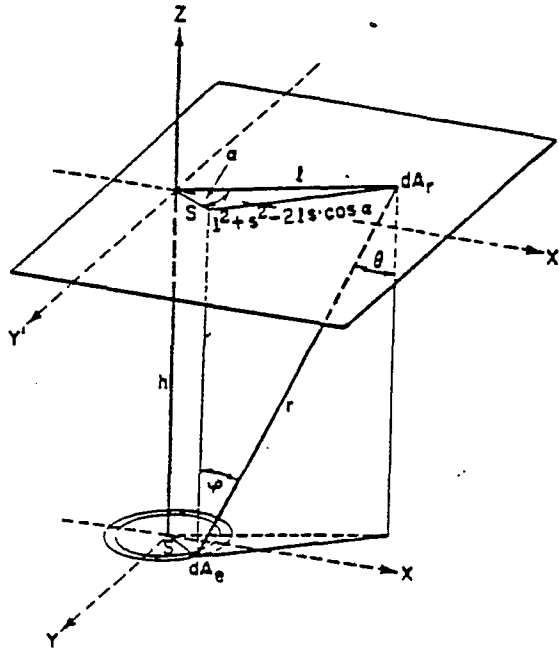


Figure E.2 Evaporation from an element  $dA_e$  of a ring to a point  $dA_r$  on the substrate plane  $X', Y'$

emitting element representing a small fraction of a thin ring may be expressed as  $dA_e = s \, d\alpha \, ds$ , where  $\alpha$  is the angle between  $l$  and the projection of  $s$  onto the substrate plane. Since the latter is parallel to the source plane,  $\cos\theta = \cos\phi = h/r$ , where  $h$  is the distance between the two planes. Substituting this relationship and Eq. E.1 into the point source Eq. E.3, the thickness received from a disk source is given by

$$d = \iiint_{t \, s \, \alpha} \frac{T s \, d\alpha \, ds \, h^2}{\pi \rho \, r^4} \, dt \quad (E.4)$$

After substituting the evaporation distance  $r$  by quantities which characterize the position of the receiving point relative to the source,  $r^2 = h^2 + l^2 + s^2 - 2ls \cos\alpha$  ( see

figure E.2), integration over  $\alpha$  from 0 to  $2\pi$  results in the expression

$$d = \int_t \int_s \frac{2Th^2}{\rho} \frac{h^2 + R^2 + s^2}{[(h^2 - R^2 + s^2)^2 + (2lh)^2]^{1/2}} s ds dt \quad (E.5)$$

In order to get the thickness distribution for circular-disk sources, Eq. (E.5) must be integrated over the disk radius  $s$ . Integration by parts yields

$$d = \int_t \frac{T}{2\rho} \left[ 1 - \frac{h^2 + R^2 - s^2}{[(h^2 - R^2 + s^2)^2 + (2lh)^2]^{1/2}} \right] dt \quad (E.6)$$

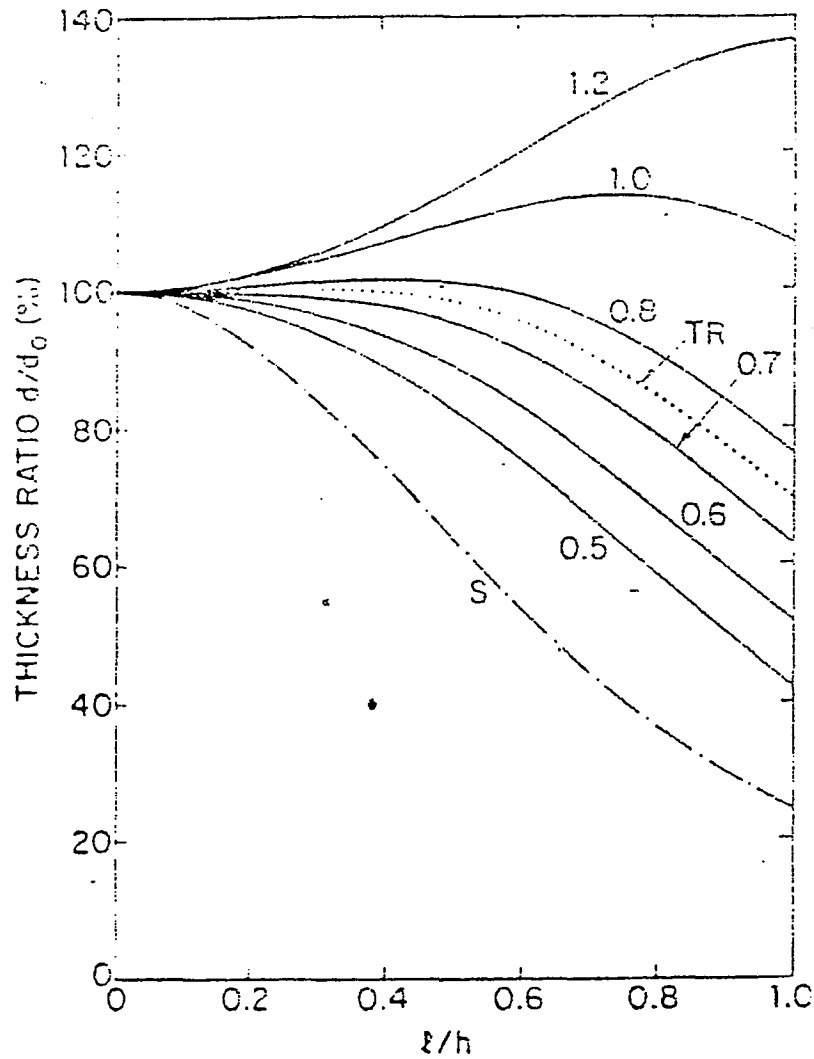
In this case, the total evaporated mass  $M_\theta$  can be substituted for  $T$  according to  $M_\theta = \pi s^2 \int_t T dt$ , which gives the thickness expressions for circular-disk sources:

$$d = \frac{M_\theta}{2\pi \rho s^2} \left[ 1 - \frac{1 + (lh)^2 - (s/h)^2}{\{ [1 - (lh)^2 + (s/h)^2]^2 + 4(lh)^2 \}^{1/2}} \right] \quad (E.7)$$

and

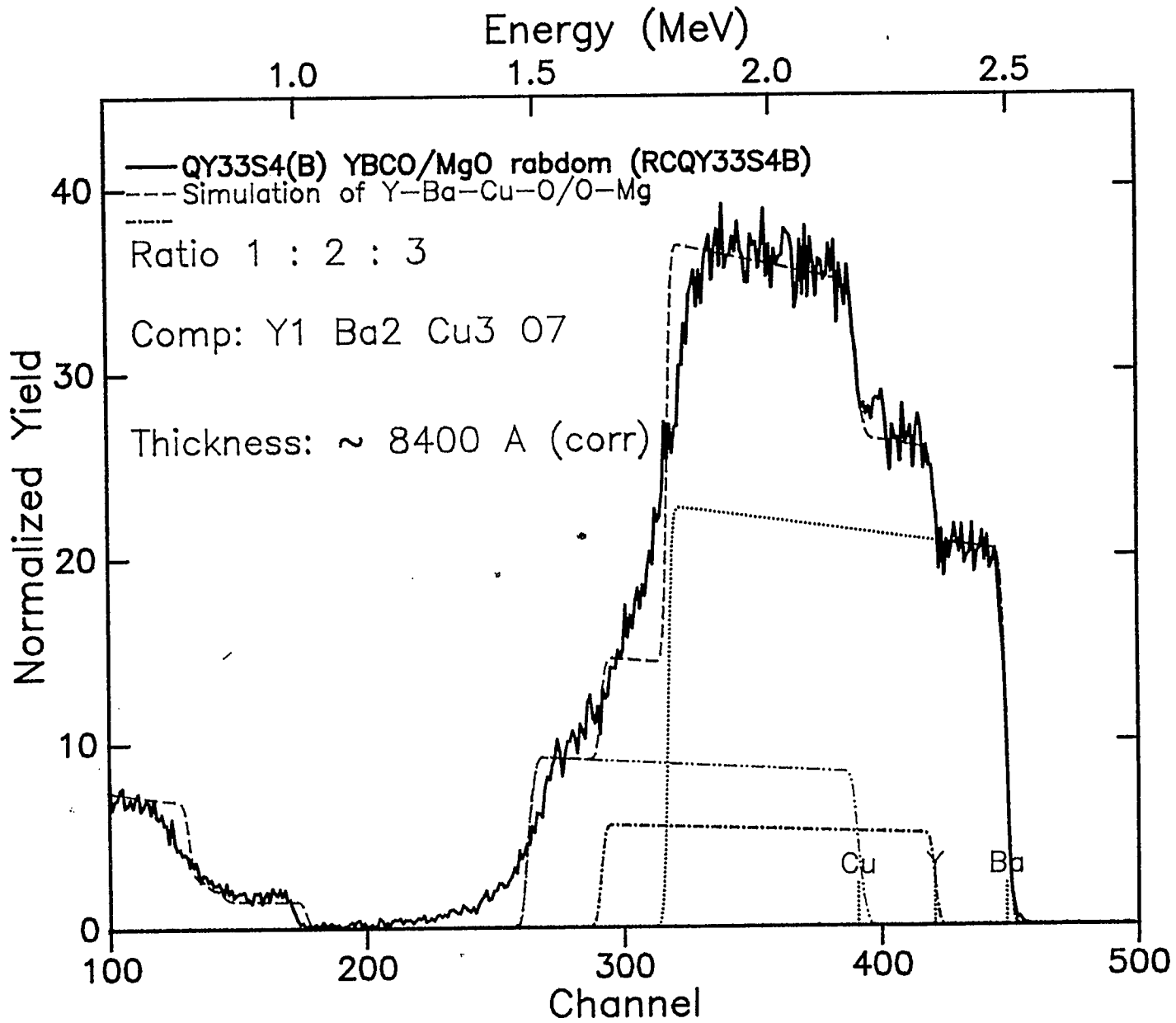
$$do = \frac{M_\theta}{2\pi \rho s^2} \frac{2(s/h)^2}{1 + ((s/h)^2)} \quad (E.8)$$

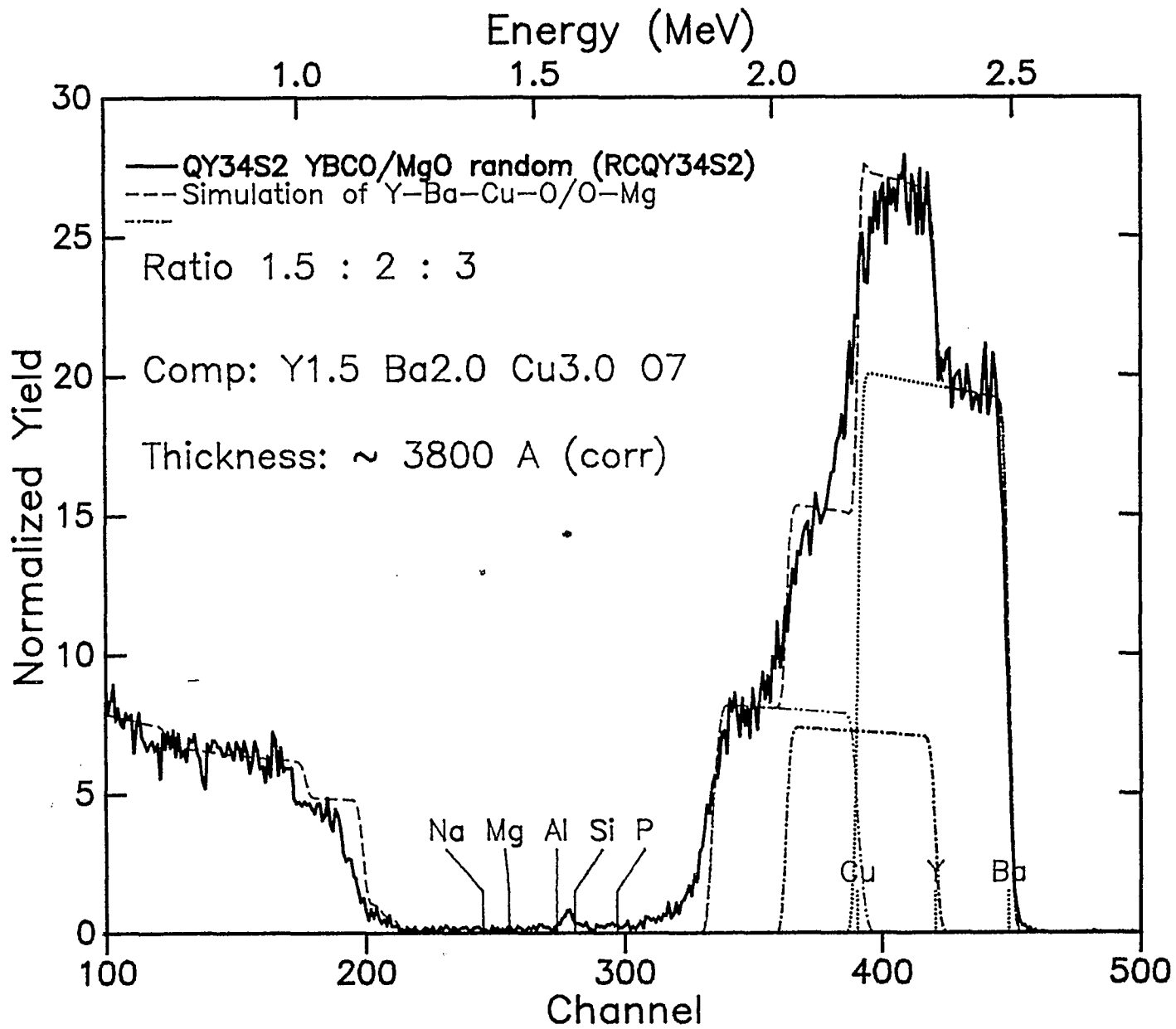
where  $do$  is the thickness at  $l=0$ .



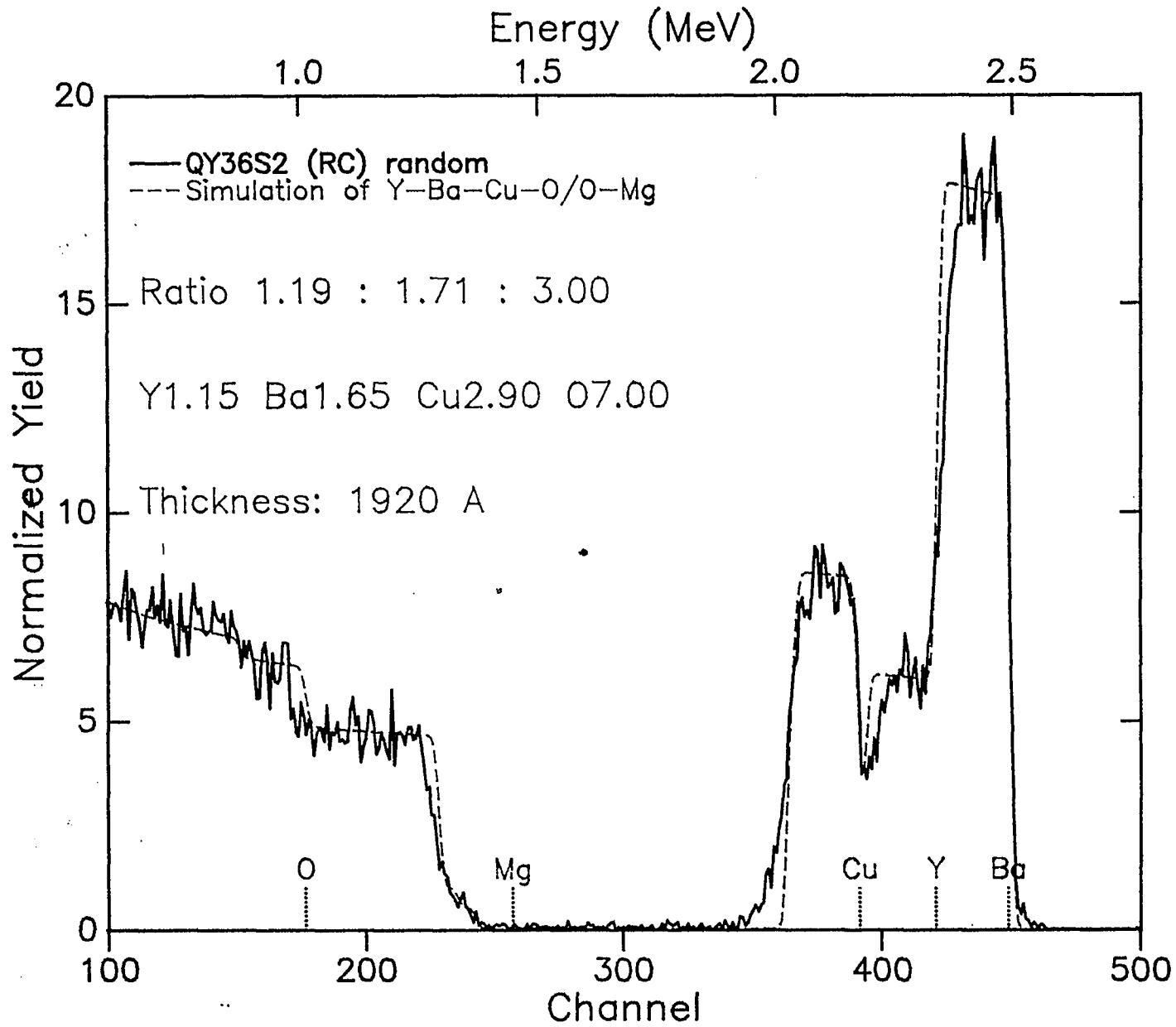
Film-thickness distributions for a small-surface source ( $S$ ) and for infinitesimally thin ring-surface sources (drawn lines). The numbers indicate the ratios of source radius  $a$  to shortest evaporation distance  $h$ . The dotted curve  $TR$  represents a ring source of finite dimensions with an inner radius  $s_i = 0.7h$  and an outer radius  $s_o = 0.8h$ .

## APPENDIX B





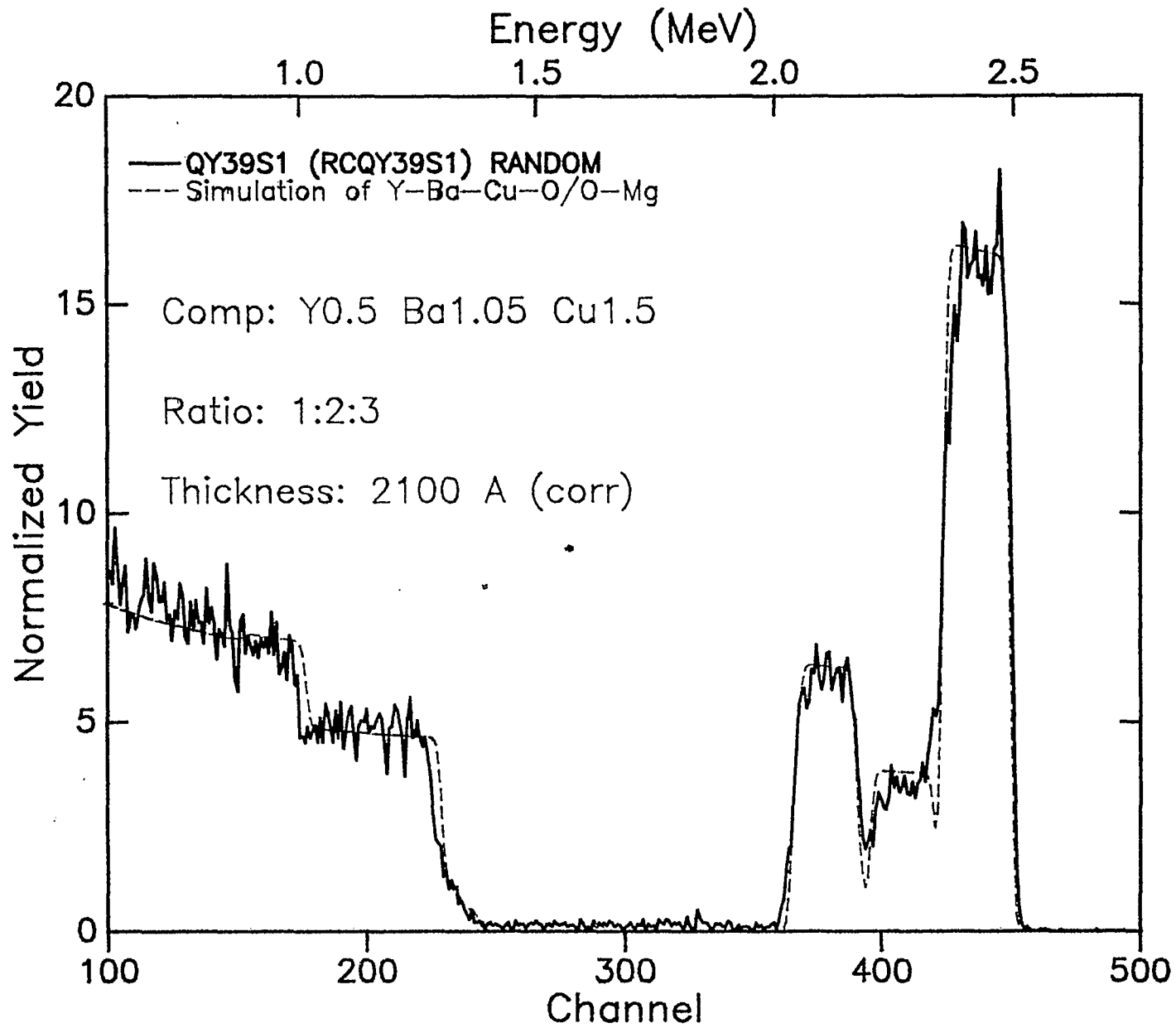
Center of sample

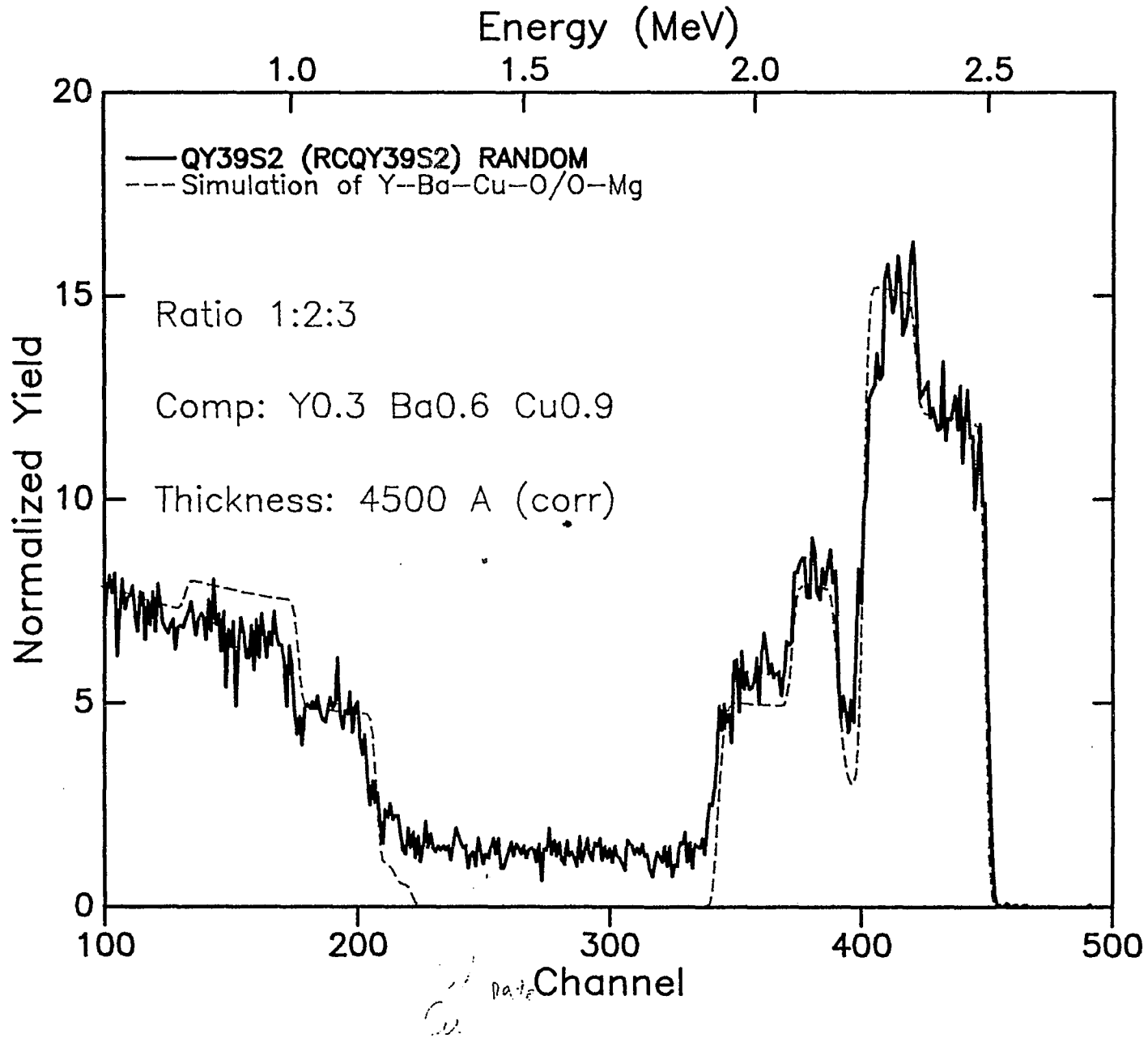


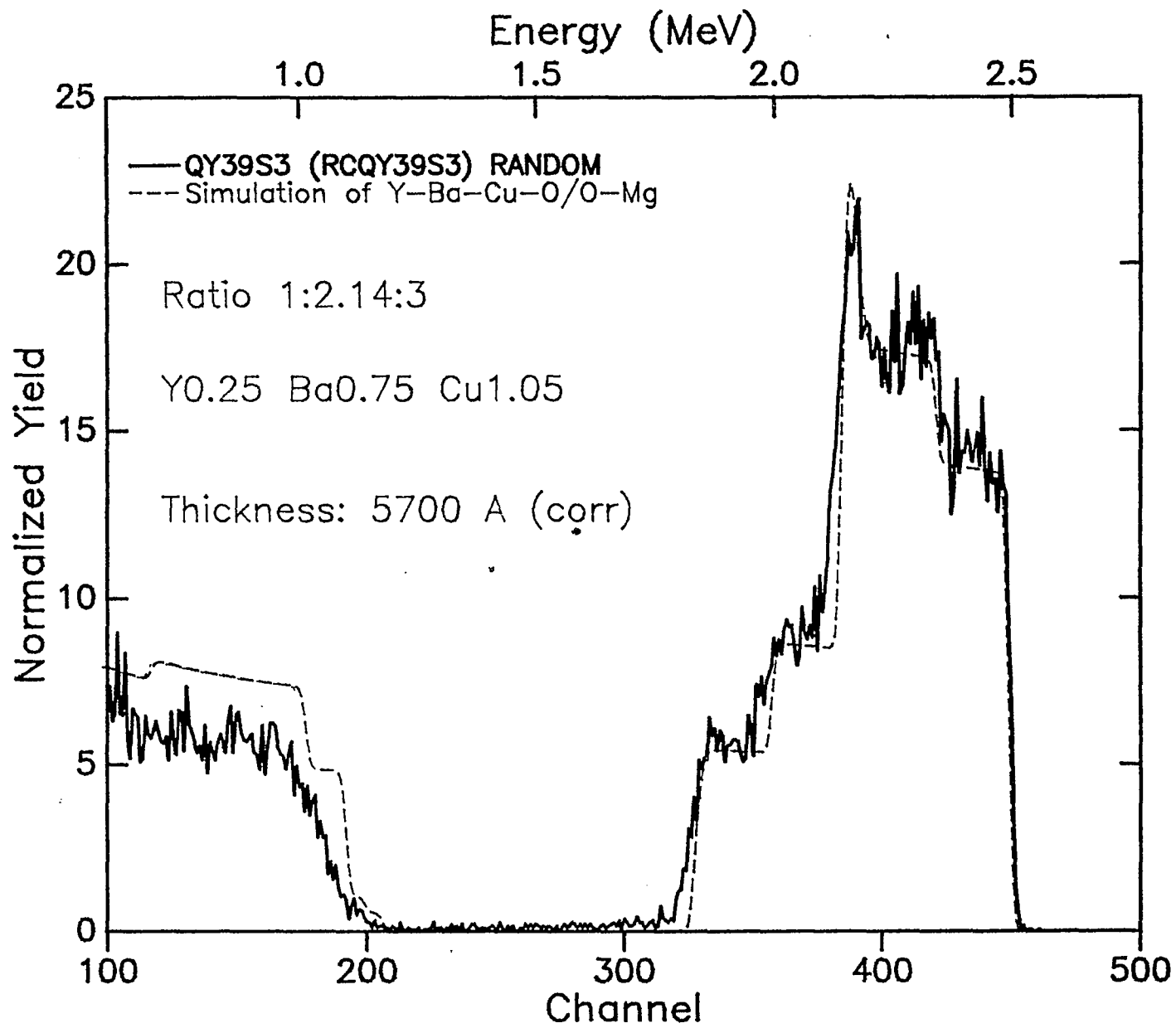
perfect crystal - Channeling get 2.5% for channel to random  
diffusion power.

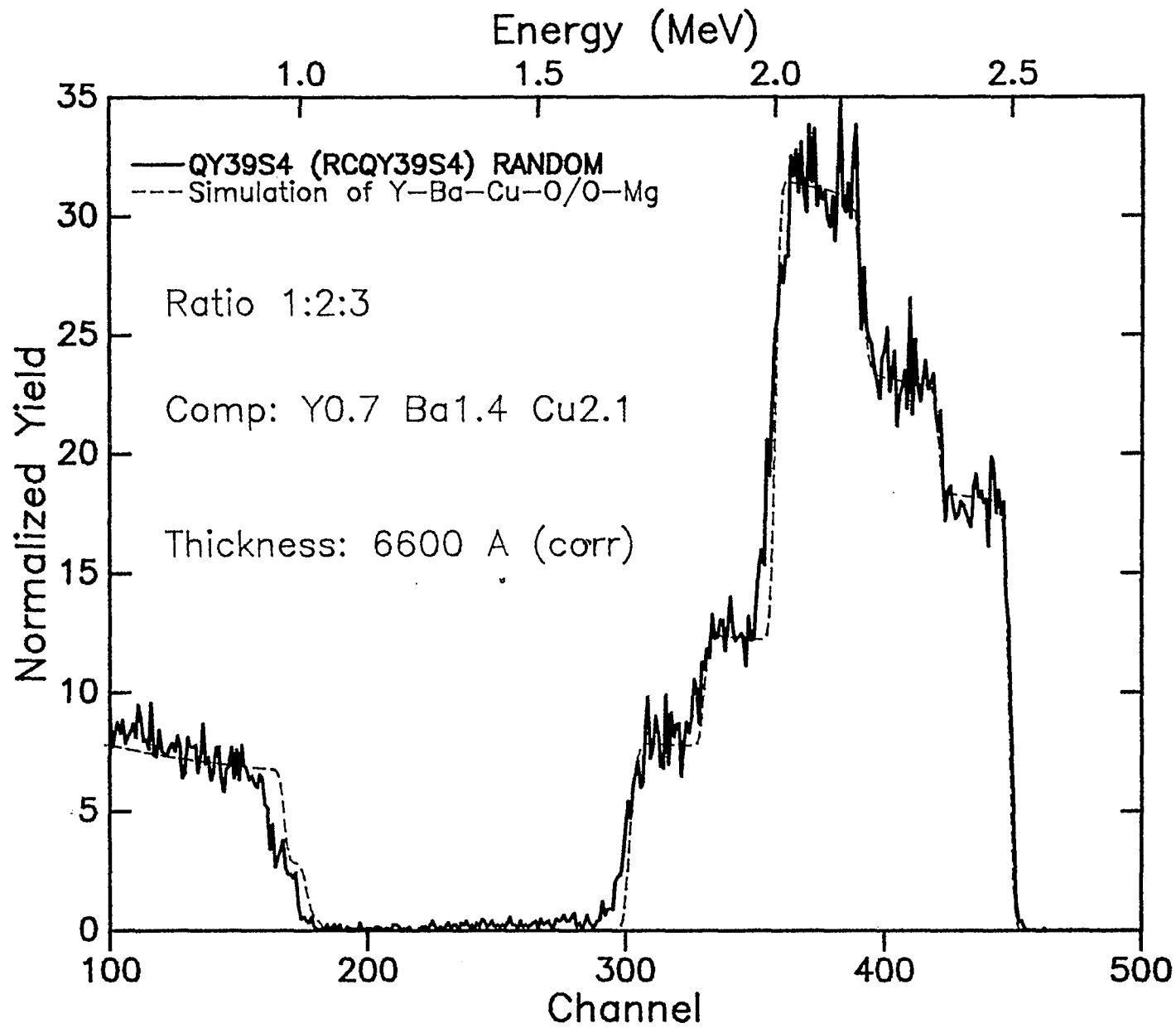
## APPENDIX C

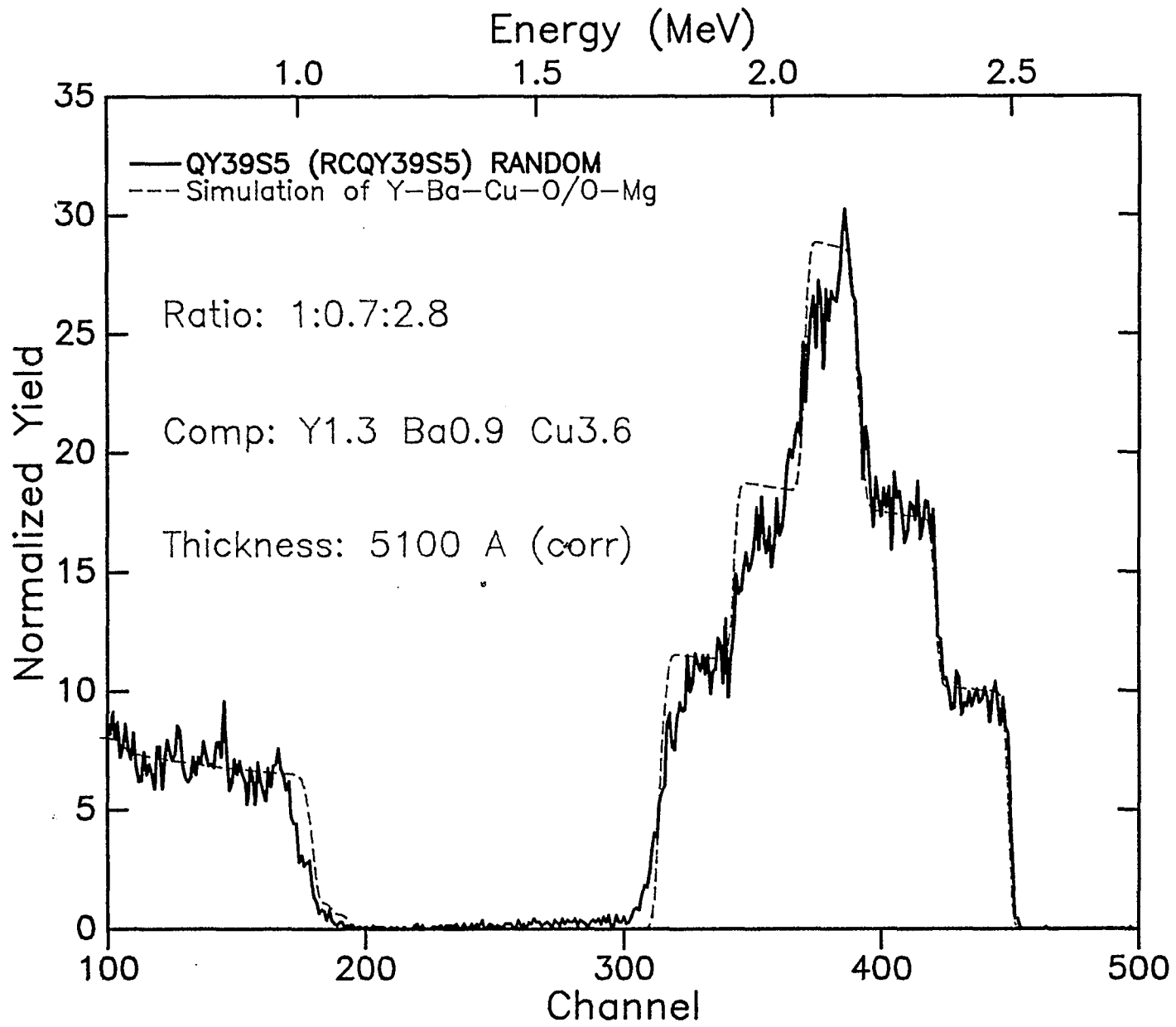


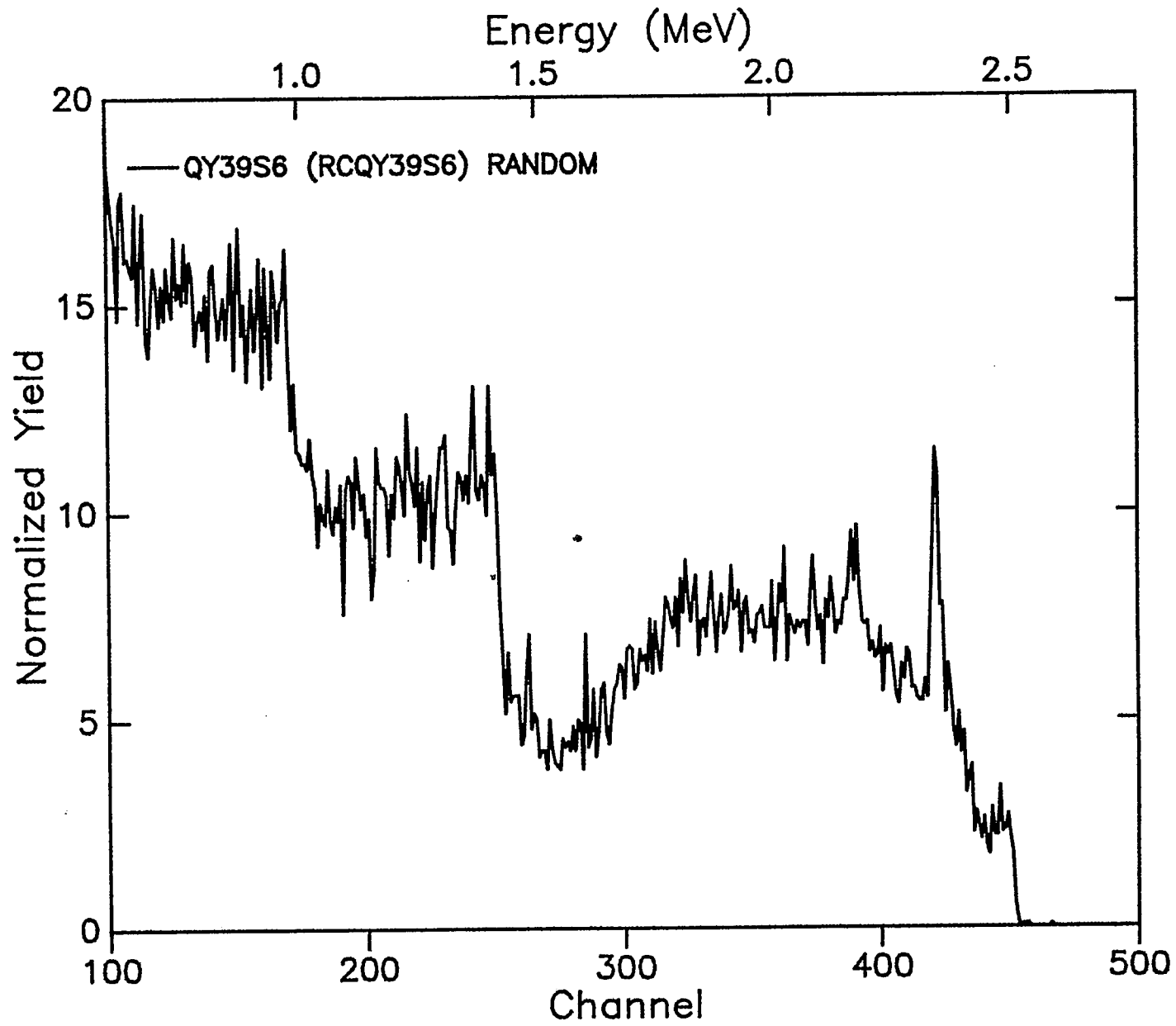




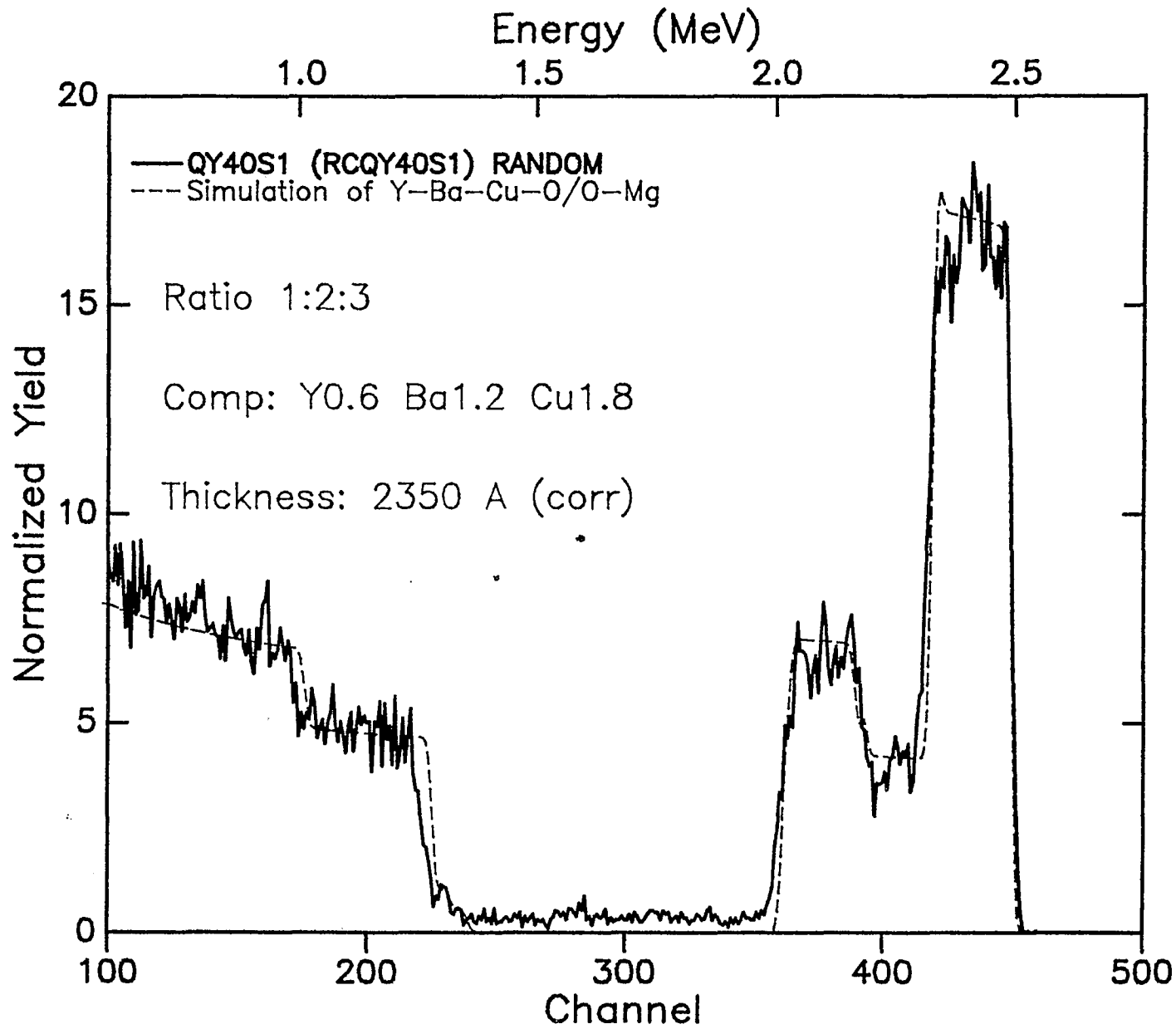




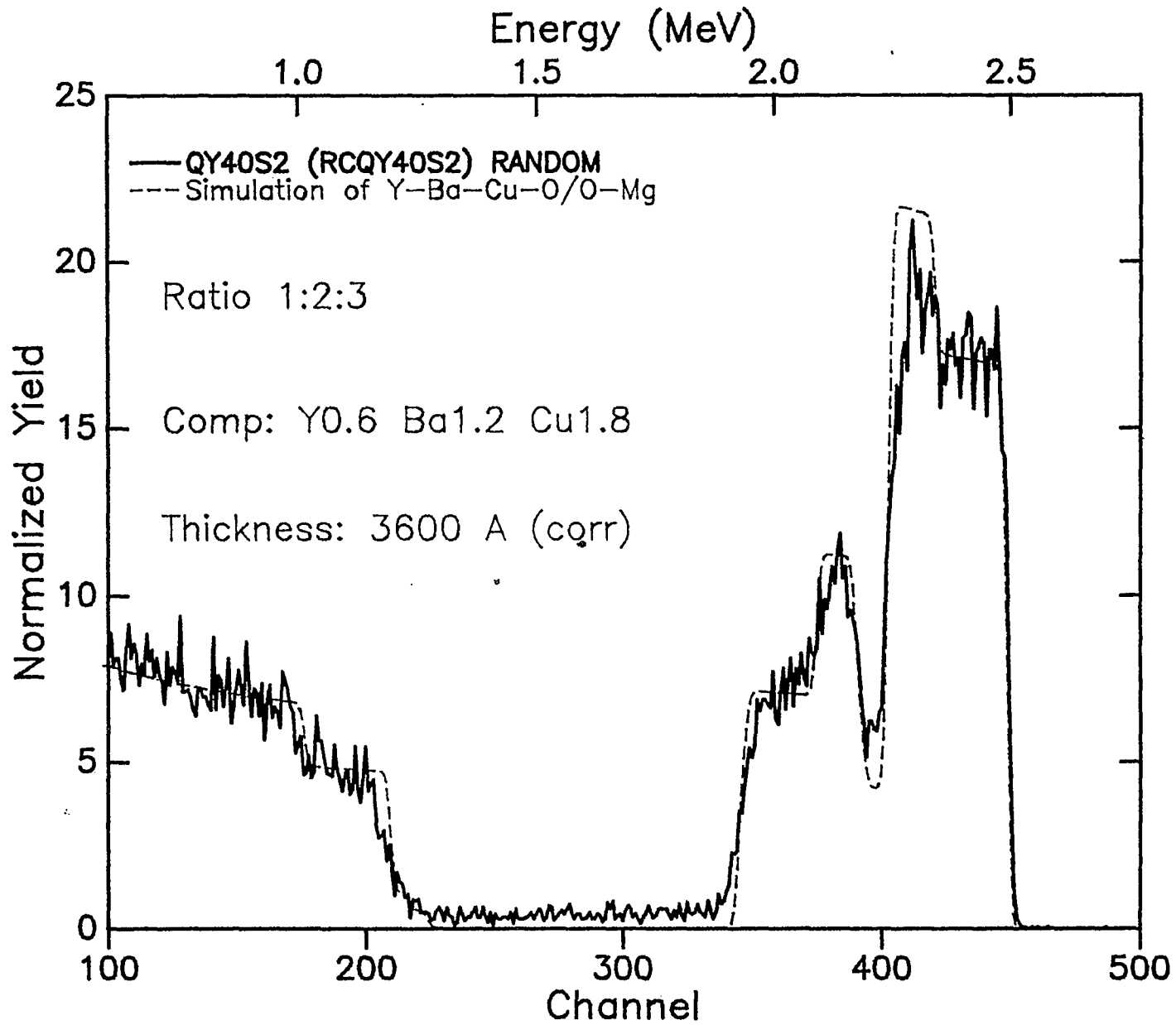


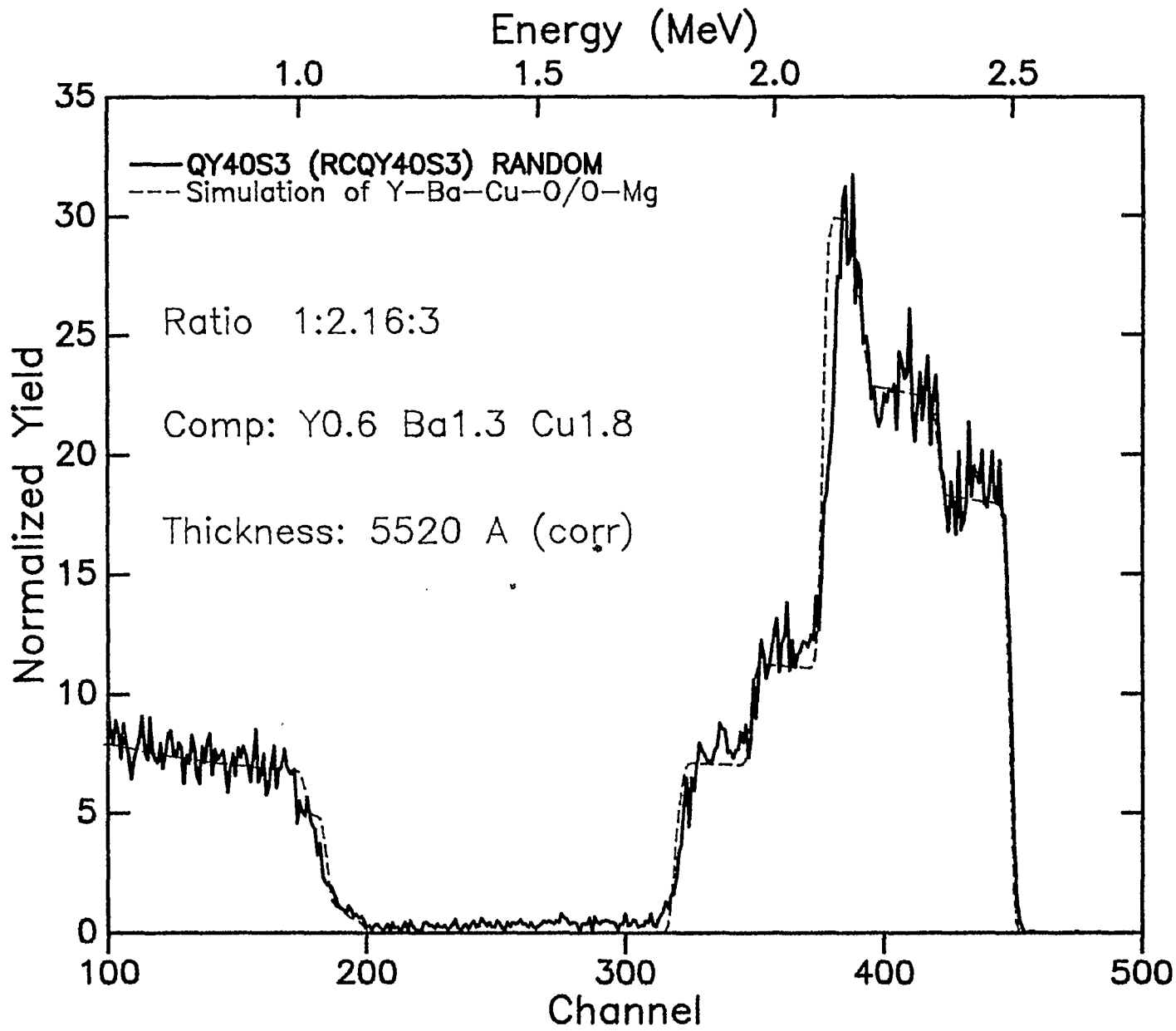


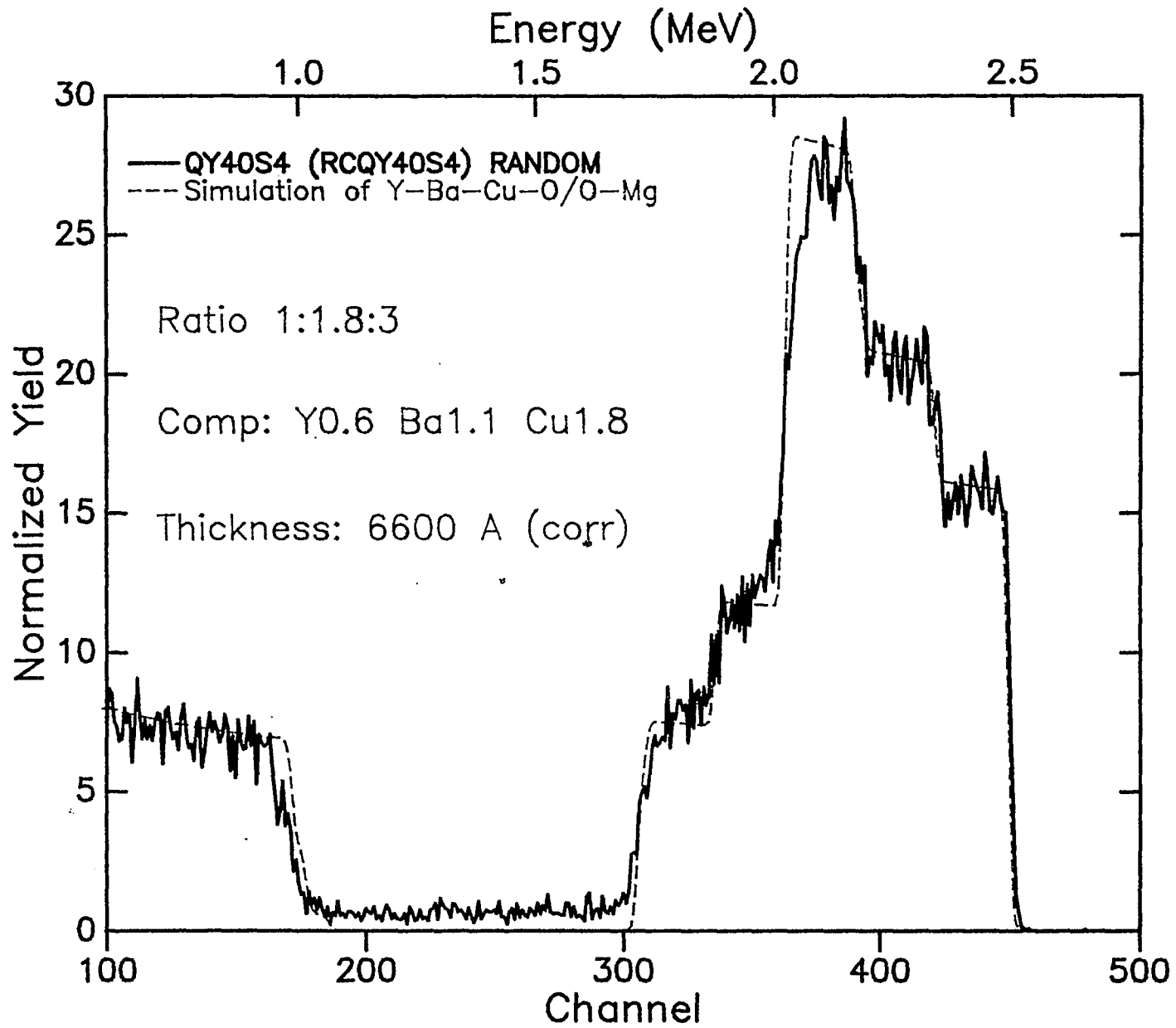
## APPENDIX D

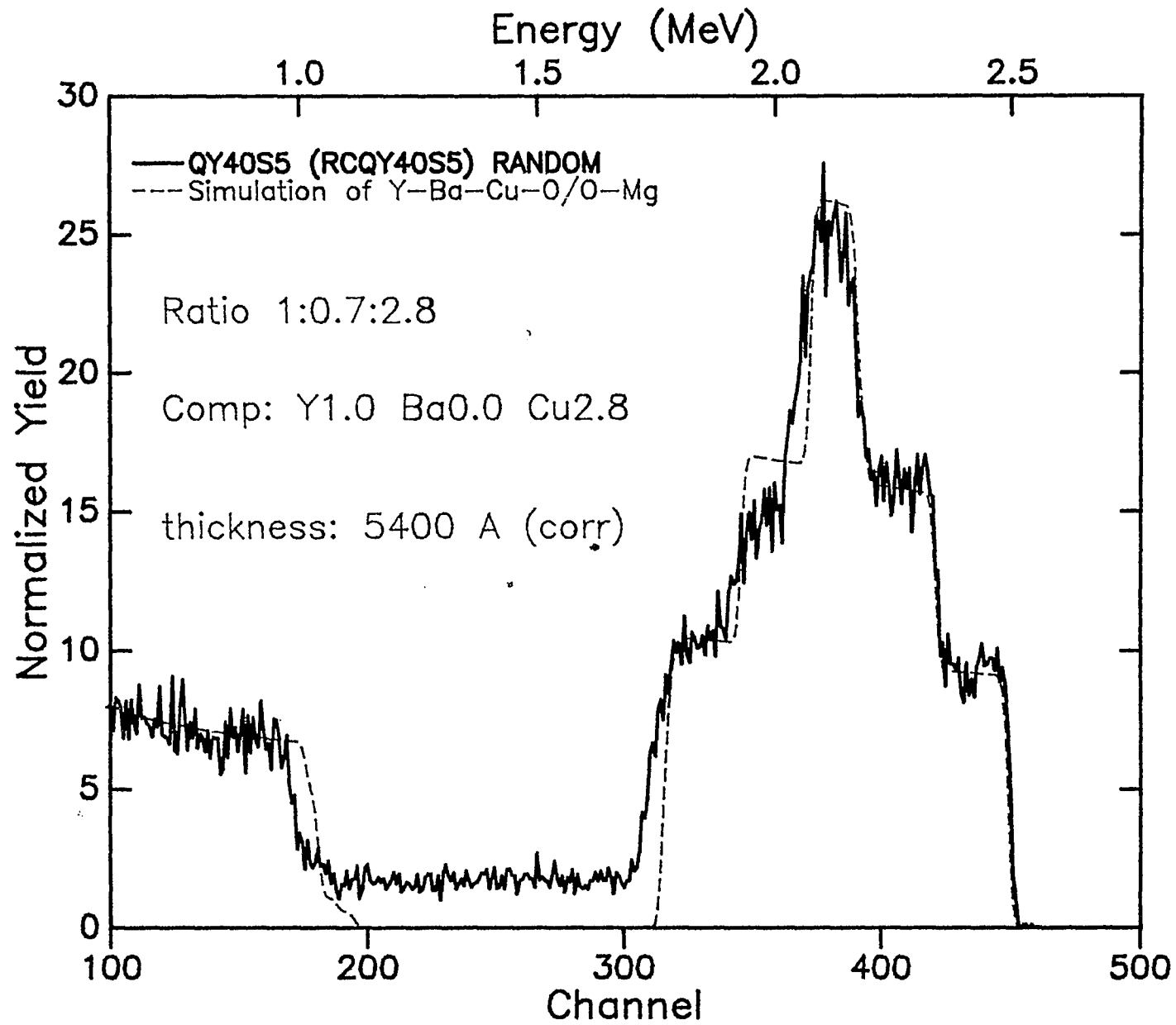


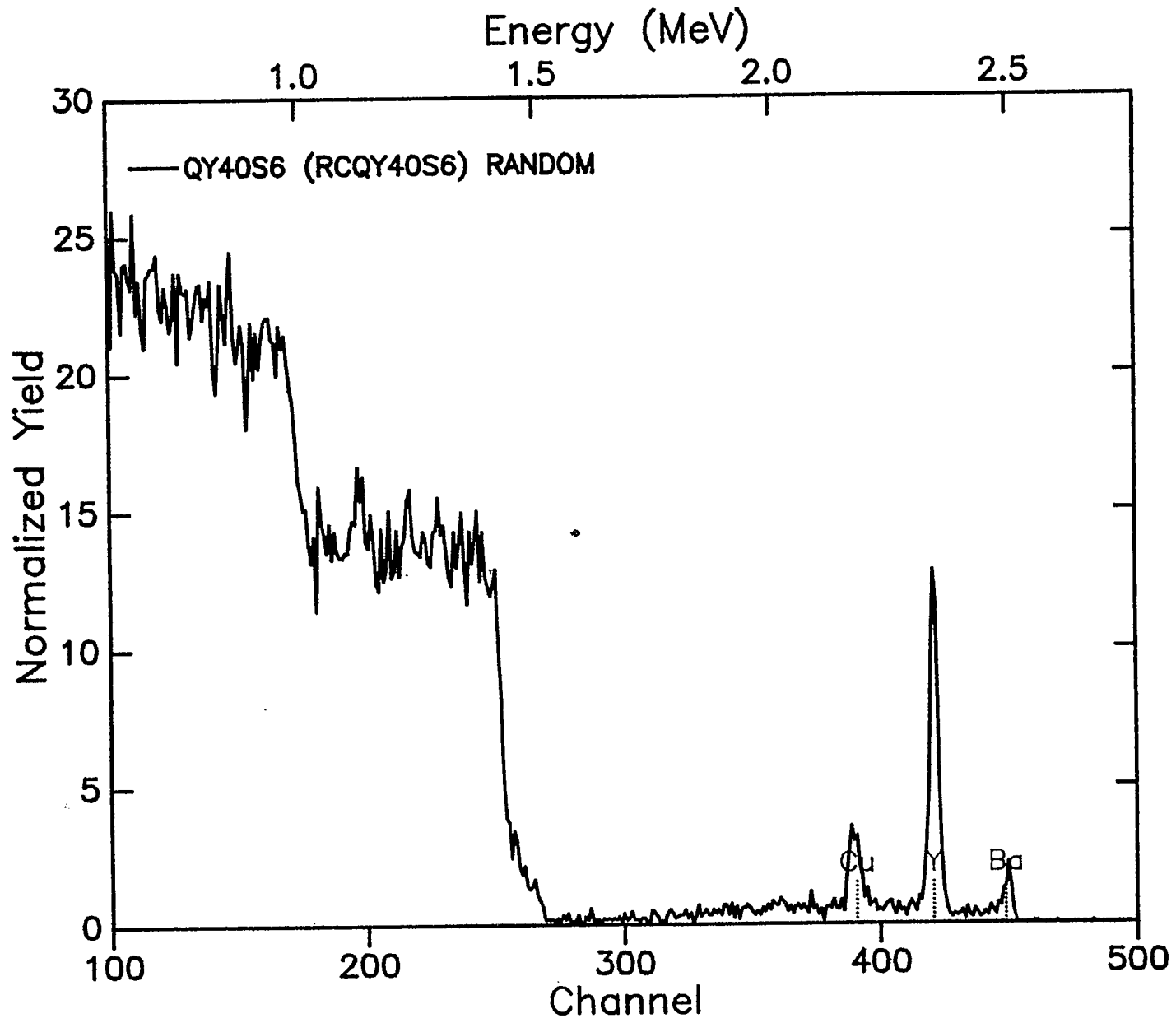




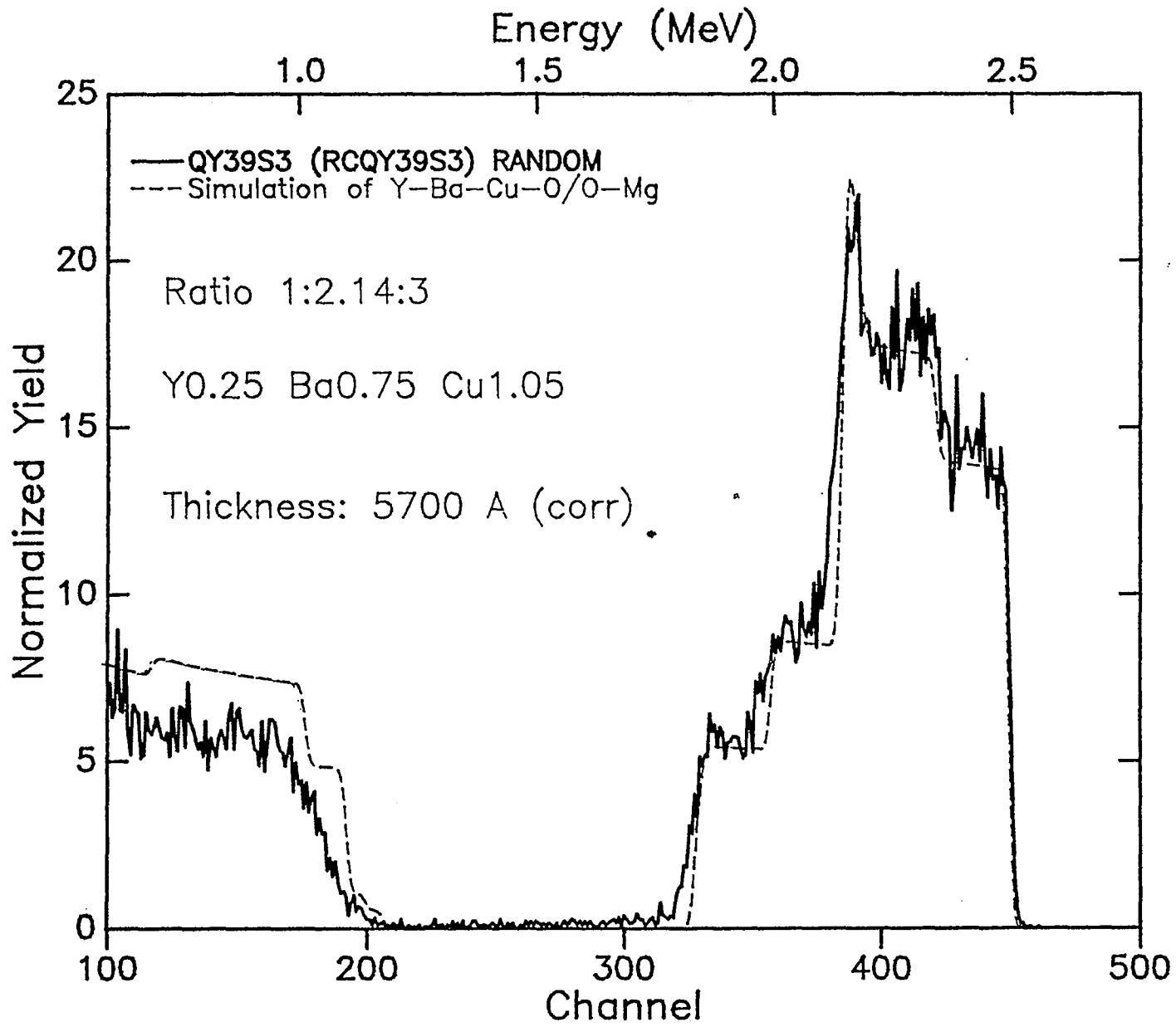


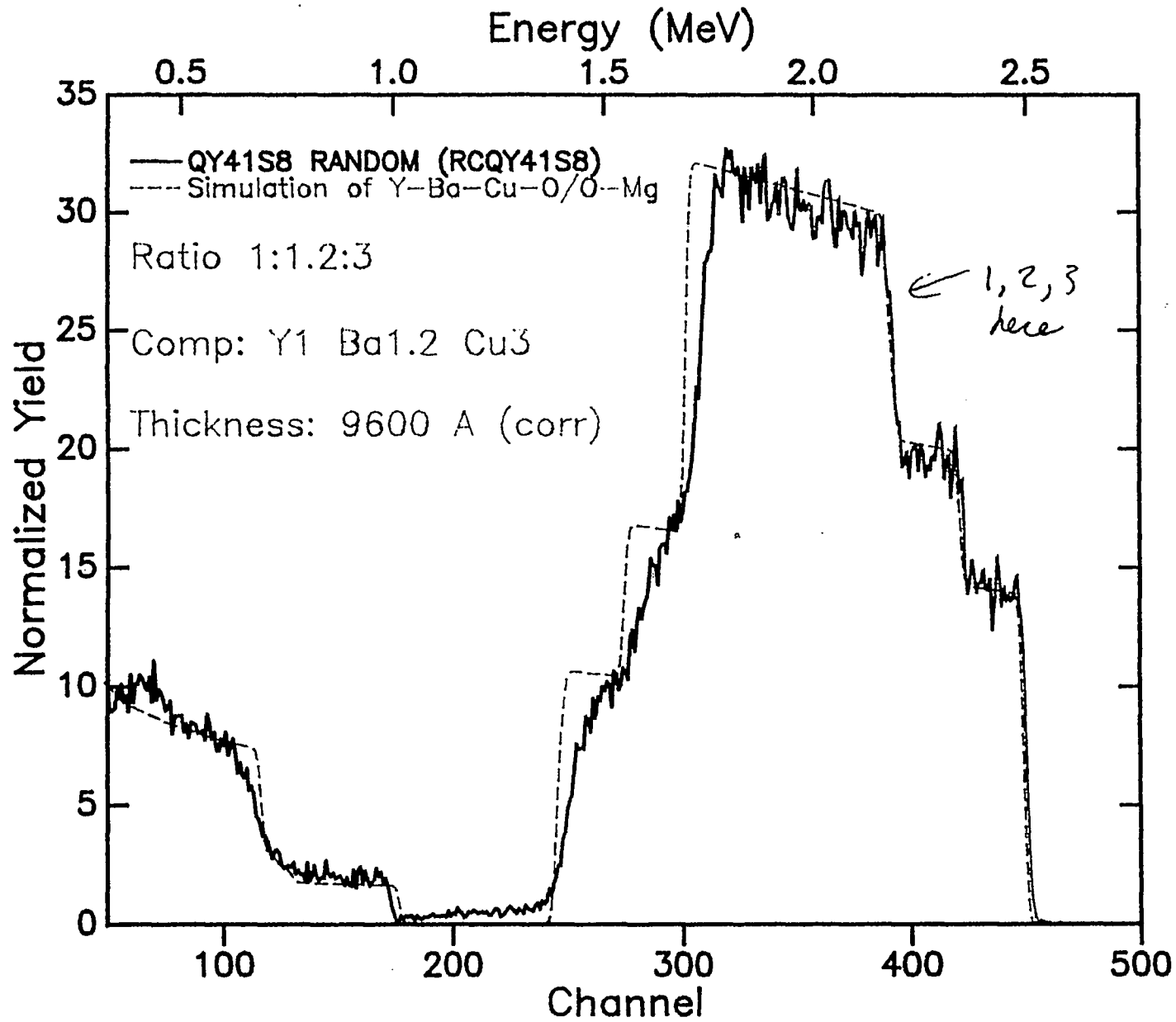






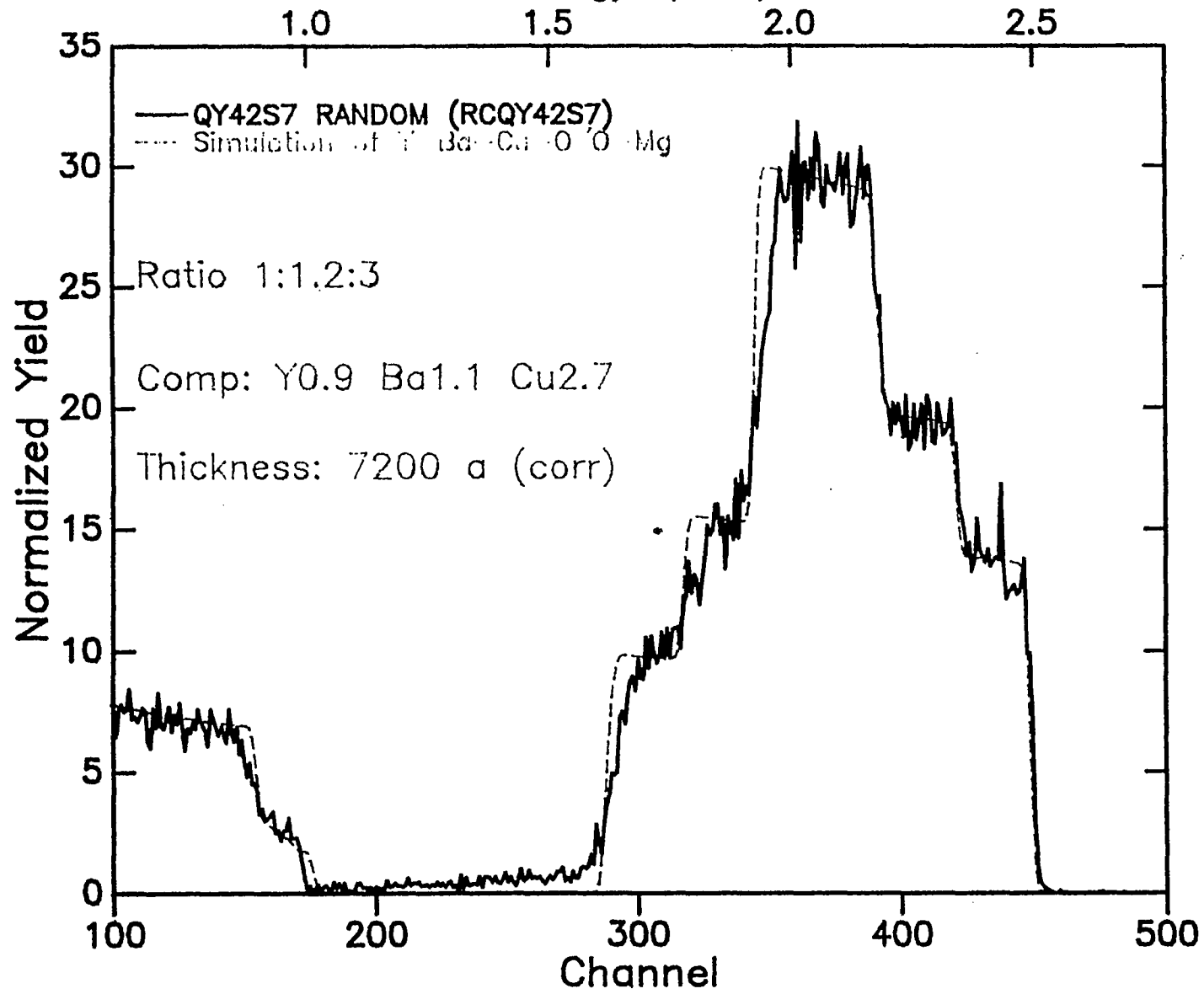
## APPENDIX E







Energy (MeV)



## APPENDIX F

